J. Fluid Mech. (2006), *vol.* 562, *pp.* 445–475. © 2006 Cambridge University Press
doi:10.1017/S0022112006001169 Printed in the United Kingdom

The effects of gravity modulation on fluid mixing. Part 1. Harmonic modulation

By V. K. SIDDAVARAM AND G. M. HOMSY

Department of Mechanical Engineering, University of California, Santa Barbara, CA 93106-5070, USA

(Received 8 July 2005 and in revised form 3 February 2006)

We study the effects of gravity modulation on the mixing characteristics of two interdiffusing miscible fluids initially in two vertical regions separated by a thin diffusion layer. We formulate the case of general gravity modulation of arbitrary orientation, amplitude g and characteristic frequency ω. For harmonic vertical modulation in two dimensions, the time-dependent Boussinesq equations are solved numerically and the evolution of the interface between the fluids is observed. The problem is governed by six parameters: the Grashof number, $Gr = (\Delta\rho/\bar{\rho})g(l_v^3/\nu^2)$, based on the viscous length scale, $l_v = \sqrt{\nu/\omega}$; the Schmidt number, $Sc = \nu/D$; the aspect ratio, A; the non-dimensional length of the domain, l; the steepness of the initial concentration profile, δ; and the phase angle of the harmonic modulation, ϕ. When $\phi = 0,\ \pi$, we observe four different flow regimes with increasing Gr: neutral oscillations at the forcing frequency; successive folds which propagate diffusively; localized shear instabilities; and both shear and convective instabilities leading to rapid mixing. In the last regime, the flow is disordered but not chaotic. By varying Sc, it was determined that the mechanism for the formation of these shear and convective instabilities is inertial. When $\phi \neq 0$ or π, the flow is similar to a modulated lock exchange flow.

1. Introduction

Mixing plays an important role in many engineering applications. Some processes try to suppress mixing, while many others try to enhance it. A few of the applications in which mixing is important are heat transfer, gas dispersion, chemical reactions including combustion, and nucleation and growth of colloidal systems. In many of the processes listed above buoyancy associated with Earth's gravity plays a major role in mixing fluids efficiently. In the microgravity environment such a mechanism is typically absent or of very little importance. For example, in the case of boiling in Earth's gravity, the heat transport is enhanced by the convective mixing associated with buoyant rise of bubbles, a mechanism that is essentially absent in the microgravity environment. Combustion is another such example that involves buoyancy forces resulting from large density differences. These buoyancy forces are of a much smaller magnitude in the microgravity environment.

Jules *et al.* (2002) found that the microgravity environment, e.g. that aboard the International Space Station (ISS), is characterized by low mean accelerations which are $O(10^{-6})\ g_e$ (g_e is the gravity on Earth) and fluctuations that are two or three orders of magnitude above the mean, i.e. $O(10^{-4} - 10^{-3})\ g_e$. Thomson *et al.* (1997) analysed the data collected during the NASA SL-J mission that flew on September 13–20, 1993 and found that the typical acceleration field consists of periodic components,

https://doi.org/10.1017/S0022112006001169 Published online by Cambridge University Press

random components with small auto-correlation time, and a white noise background. These gravity fluctuations are collectively termed gravity jitters or g-jitter. Gravity jitters interact with density and concentration gradients resulting in time-dependent, three-dimensional body forces, generating a flow. An illustration of the effects of flows caused by g-jitter can be found in the experiments of Radcliffe *et al.* (1988) who attempted to grow organic crystals in Low Earth orbit. The quality of the crystals grown was poorer than expected, which was attributed to the effects of g-jitter. In these and other applications, it is therefore important to understand the nature of the flows generated by g-jitter.

There is a small but significant literature on g-jitter convection. Gresho & Sani (1970) studied the effect of a time-modulated vertical gravity field on the Rayleigh–Bénard instability of a heated fluid layer and concluded that the effect of gravity modulation is to change the critical Rayleigh number. In particular, a layer of fluid heated from above, which is normally stable because of the stable density stratification, may be destabilized by gravity modulation and a layer of fluid heated from below may be stabilized. They also noted that this result is analogous to the stabilization of an inverted pendulum by suitable vertical oscillations of the pivot. These results were observed experimentally by Rogers *et al.* (2000) and confirmed numerically by the three-dimensional studies of Biringen & Peltier (1990).

Many recent studies have focused on the effect of jitter on convective flows driven by mean gravity, e.g. Farooq & Homsy (1996), Chen & Chen (1999), and Christov & Homsy (2001). The model problem of choice for most of these investigations was convection in an infinite vertical slot with differentially heated walls. The main advantage of this model is that it provides the context of a relatively simple base flow in which to study the instabilities observed in more complicated situations. Some studies, e.g. Chen & Chen (1999), exclude any vertical stratification, whereas others, e.g. Farooq & Homsy (1996), include it. When vertical stratification is excluded the horizontally stratified problem has an exact linear parallel flow solution with no potential for parametric instability. The inclusion of vertical stratification, while still admitting a parallel flow, has the potential for parametric instability. Chen & Chen (1999) observed synchronous and sub-harmonic instability modes for a low-Prandtl-number fluid and quasi-periodic and sub-harmonic instability modes for a high-Pr fluid. From the kinetic energy analysis of the perturbation for a low-Pr fluid they found that the dominant contribution comes from the transfer of energy from the mean flow to the disturbance due to Reynolds stresses. Therefore the instabilities are essentially driven by viscous shear. By a similar analysis for a high-Pr fluid they found that the instabilities are buoyancy driven. They also observed that gravity modulation can either stabilize or destabilize the flow.

Farooq & Homsy (1996) studied the effect of gravity modulation on vertical slots with both horizontal and vertical stratification. There are three types of modes in the absence of gravity modulation: travelling modes associated with the instability of the boundary layers on the sidewalls, internal gravity waves associated with the vertical density stratification, and stationary convective modes. When the jitter is weak, they found resonant interactions with the natural modes of the unmodulated problem which lead to a shift in the critical Rayleigh numbers. When the jitter is of the same magnitude as the mean gravity, they found that the parallel-flow modes can be destabilized by gravity modulation. They observed parametric instability for sufficiently large modulation amplitude. They noted that the parallel-flow equations do not have any nonlinear saturation mechanisms, which allows the solution to grow without bound. To circumvent this difficulty they analysed a reduced-order (two

https://doi.org/10.1017/S0022112006001169 Published online by Cambridge University Press

mode) nonlinear model and observed nonlinear coupling between the two modes which leads to saturation. Christov & Homsy (2001) considered this problem in more detail by solving the full nonlinear Boussinesq equations numerically. They found that the nonlinear two-dimensional solutions for the case of steady gravity agree well with the linear stability calculations of Bergholz (1978). They too observed parametric instability when the modulation amplitude was sufficiently large. From an energy analysis, they concluded that phase lag between the flow and temperature responses due to fluid inertia is the primary mechanism of the parametric instability. They discovered the existence of a parameter-independent two-dimensional flow structure that is responsible for stabilization of the unstable one-dimensional flow. They found that jitter is strongly coupled with the vertical stratification, exciting Rayleigh–Bénard modes for unstable stratification and suppressing the instability modes for stable stratification.

Studies have also been done for the case when the gravity vector orientation is parallel to that of the thermal gradient. Lizée & Alexander (1997) studied the thermovibrational flow in a laterally heated cavity subject to large-amplitude harmonic horizontal accelerations. They find a sequence of period-doubling bifurcations as the jitter amplitude is varied, leading to chaotic regimes at large amplitudes.

In a study that provides much of the motivation for the current work, Duval & Jacqmin (1990) considered the g-jitter convection of two diffusing miscible liquids of differing densities under an oscillating vertical gravitational field with zero mean. When the density difference between the fluids is small, they observed that the long-time mixing is dominated by mass diffusion. They also found that over the time considered, the diffusion layer remains sharp and undeformed. Although the fluids are miscible, we refer to this layer as an 'interface'. For large density differences they identified two types of instabilities: Kelvin–Helmholtz instability associated with the growth and oscillation of the interface, and 'chaotic instability' associated with the breakup of the interface. Chaotic instability occurs when a parameter (which they call the 'Stokes-Reynolds number') exceeds a critical value of 5.25. This Stokes-Reynolds number corresponds to the Grashof number, Gr, in our study and is defined later. They observed that the interface evolves like a vortex sheet. Below the critical Stokes-Reynolds number, the destabilization of the interface through the Kelvin–Helmholtz instability results in its deformation into wavy structures. In some parametric regions, these structures oscillate in time and in others they are quasi-steady. Above the critical Stokes-Reynolds number the interface breaks into small concentration pockets. They proposed that the initial breakup of the interface occurs by means of Rayleigh–Taylor instability. Duval & Jacqmin (1990) limited their attention to a relatively narrow parameter range. In their studies, the Schmidt number, Sc, is $O(10^2)$, the Grashof number, Gr, is less than 15, and the initial phase angle, ϕ, is zero. They have not studied the effect of Sc, ϕ, and aspect ratio, A, on the critical Stokes-Reynolds number. Our study will widen this parameter range considerably with the aim of elucidating the physical mechanisms and further characterizing the flows. We vary Sc from 1 (Sc for gases is $O(1)$) to 100. Our motivation for varying Sc is to determine if the Rayleigh number, $Ra = Gr\,Sc$ is a more appropriate parameter for our studies, rather than the Grashof number, Gr. We will also vary Gr from 1 to 25, examine the dependence of the critical Stokes-Reynolds number, $Re_{S,c}$ on Sc and A, and investigate the dynamics of point quantities in order to determine whether the flow is chaotic. Finally we investigate the effect of varying the phase angle, ϕ.

Duval (1992) also studied the effect of a time-dependent gravity field on the mixing of two fluids. The gravity field consists of both steady and oscillatory components. He

https://doi.org/10.1017/S0022112006001169 Published online by Cambridge University Press

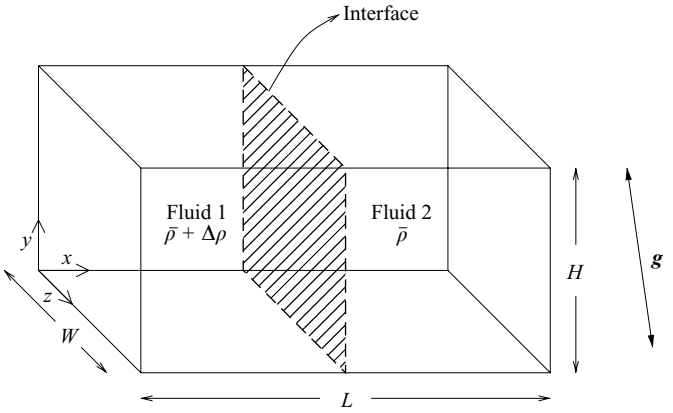

FIGURE 1. Schematic of the three-dimensional problem.

observed the formation of two distinct structures depending upon whether the gravity field is dominated by the steady component or the oscillatory component. When the steady component of the gravity dominates, the interface is deformed into a 'whorl' structure and when the oscillatory component dominates the interface is deformed into 'tendrils'. In the parametric region that he considered, two flow regimes occur: convective and chaotic. In the convective flow regime, the flow field is oscillatory, the phase-space trajectories associated with the velocities are elliptical, and the power spectrum indicates that the flow field responds at a frequency corresponding to the frequency of gravity modulation. In the chaotic regime, the flow field is aperiodic, the phase-space trajectories associated with the velocities are irregular, and the power spectrum shows a broadband response.

In all of the above studies, the gravity modulation is harmonic. Drolet & Viñals (1997) studied the problem of the onset of oscillatory instabilities under stochastic modulation and concluded that stochastic jitter may have qualitatively different effects than simple deterministic models of jitter. More specifically, they studied the effect of stochastic modulation on a system with $O(2)$ symmetry that exhibits Hopf bifurcation in the absence of modulation. The study included a random component in both the control parameter of the bifurcation and the modulation amplitude. At a Hopf bifurcation in a periodically modulated system, the trivial state loses stability to either travelling waves when the modulation amplitude is small, or standing waves when the amplitude is sufficiently large. They concluded that when the modulation amplitude has a stochastic component, the threshold for the onset of instability in the standing-wave regime is shifted from its deterministic location and the region of primary bifurcation to travelling waves disappears.

The main objective of the current study is to investigate the physical mechanisms by which g-jitter affects the mixing characteristics of two miscible fluids which initially meet at a sharp vertical interface.

2. General problem formulation

Since the aim of this study is to investigate physical mechanisms, we analyse a model problem, namely a box filled with two miscible fluids with no surface tension which initially meet at a sharp but continuous vertical interface. Figure 1 shows a schematic of the general three-dimensional problem. The gravity vector is time-dependent and

https://doi.org/10.1017/S0022112006001169 Published online by Cambridge University Press

three-dimensional. As pointed out in the introduction, gravity jitters consist of both harmonic and random components. Therefore, we want to develop a formulation that is general enough to admit both deterministic and stochastic models of gravity jitters. In the present paper we focus mainly on the effects of harmonic jitter. The effects of stochastic gravity modulation on fluid mixing will be investigated in a future article.

Without any loss of generality, we can assume that the lighter fluid, of density $\bar{\rho}$, is on the right-hand side of the cavity and the heavier fluid, of density $\bar{\rho}+\Delta\rho$, is on the left-hand side. We assume that the density difference between the fluids, $\Delta\rho$, is small, i.e. $\Delta\rho/\bar{\rho} \ll 1$ and that the following equation of state governs the two fluids:

$$\rho = \bar{\rho}(1+\beta\Delta C) \text{ where } \beta = \frac{1}{\bar{\rho}}\frac{\partial\rho}{\partial C}.$$

In the above equation, C is the concentration of the heavier fluid. Therefore, without any loss of generality we can take $C=1$ on the left boundary wall of the cavity and $C=0$ on the right boundary wall. Since we assume that the two fluids are miscible, C varies smoothly from 1 to 0 inside the cavity, i.e. the density ρ varies smoothly from $\bar{\rho}+\Delta\rho$ to $\bar{\rho}$. We now apply the Boussinesq approximation and obtain the following equations:

$$\nabla\cdot\boldsymbol{V} = 0, \tag{2.1}$$

$$\bar{\rho}\frac{\mathrm{D}\boldsymbol{V}}{\mathrm{D}t} = -\nabla p + \mu\nabla^2\boldsymbol{V} + \rho\boldsymbol{g}(t), \tag{2.2}$$

$$\frac{\mathrm{D}C}{\mathrm{D}t} = D\nabla^2 C, \tag{2.3}$$

When deriving the above equations we have also assumed that the coefficient of dynamic viscosity, μ, and the coefficient of mass diffusion, D, are independent of concentration. $\boldsymbol{V}$ is the dimensional velocity vector and p is the dimensional pressure. The gravitational field may consist of a mean and a fluctuating part

$$\boldsymbol{g} = \bar{\boldsymbol{g}} + \boldsymbol{g}'.$$

We pick a characteristic time scale, T, based on the power spectrum of $g(t)$, where $g(t)$ is the magnitude of the gravity vector, i.e. $g(t)=|\boldsymbol{g}(t)|$. When the gravity modulation is deterministic we choose $T=1/\omega$, where ω is the frequency at which the power spectrum response of $g(t)$ is assumed to have a maximum. When the gravity modulation is stochastic (to be considered in a future paper) we choose the time scale based on the form of the autocorrelation of $g(t)$, which is assumed to have a structure allowing a characteristic frequency to be defined. The length scale is chosen as the viscous length, $l_\nu=\sqrt{\nu/\omega}$, where $\nu=\mu/\bar{\rho}$ is the kinematic viscosity. The velocity scale is chosen as the buoyancy velocity, $U_c=(\Delta\rho/\bar{\rho})(g/\omega)$. Here g is the characteristic scale of $g(t)$, i.e. the maximum magnitude of the gravity vector, $|g(t)|_{max}$, when the modulation is deterministic and the standard deviation of $g(t)$ when the modulation is stochastic. This particular choice of the velocity scaling was obtained after an order of magnitude analysis of the momentum equation and equating the magnitudes of the viscous diffusion and buoyancy force terms. Velocity, distance, time, and pressure are scaled using U_c, l_ν, $1/\omega$, and $\bar{\rho}U_c^2$ respectively. For notational simplicity, we use the same variables for both the non-dimensional and dimensional variables. The resulting non-dimensionalized equations are

$$\nabla\cdot\boldsymbol{V} = 0, \tag{2.4}$$

https://doi.org/10.1017/S0022112006001169 Published online by Cambridge University Press

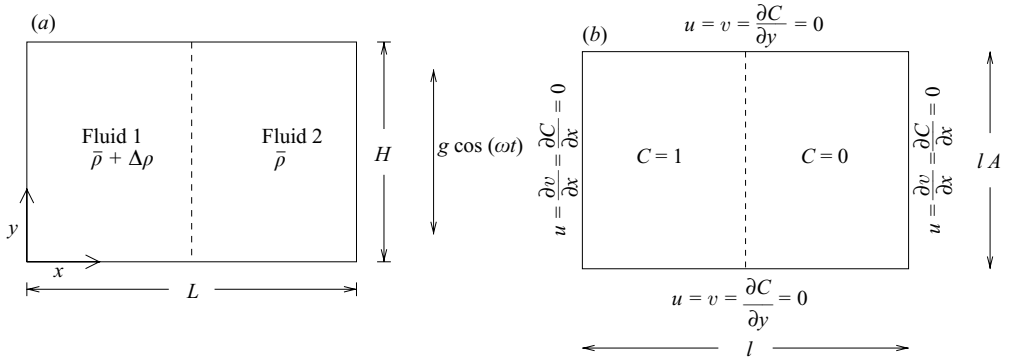

FIGURE 2. Schematic of (*a*) the two-dimensional problem (*b*) the initial and boundary conditions in dimensionless terms.

$$\frac{\partial \boldsymbol{V}}{\partial t} + Gr\boldsymbol{V}\cdot\nabla\boldsymbol{V} = -Gr\nabla p + \nabla^2\boldsymbol{V} + \frac{\rho}{\Delta\rho}(\bar{\boldsymbol{g}} + \boldsymbol{g}'), \tag{2.5}$$

$$\frac{\partial C}{\partial t} + Gr\boldsymbol{V}\cdot\nabla C = \frac{1}{Sc}\nabla^2 C. \tag{2.6}$$

In the above equations

$$Gr = \frac{U_c T}{l_v} = \frac{\Delta\rho}{\bar{\rho}}\frac{g}{\nu^{1/2}\omega^{3/2}} = \frac{\Delta\rho}{\bar{\rho}}g\frac{l_v^3}{\nu^2}$$

is a Grashof number, $Sc = \nu/D$ is the Schmidt number, and $\boldsymbol{g}$ is scaled as described above. Ratios of gravitational accelerations (g_x', $\bar{g}_x$, ...) also appear in the equations. Additional parameters are introduced into the problem through the boundary conditions, which are the non-dimensionalized length of the domain, $l = L/l_v$ and the aspect ratios ($A = H/L$ and $A_2 = W/L$).

3. Two-dimensional vertical harmonic gravity

Since we are interested in a physical understanding of the phenomenon of mixing, we reduce the complexity of the problem by focusing our attention, at present, on two-dimensional effects, i.e. $w = \partial()/\partial z = 0$, and assuming that the gravity is entirely in the vertical direction, i.e. $\bar{g}_x = \bar{g}_z = g_x' = g_z' = 0$. Since g-jitter is characterized by low mean and large fluctuations we assume that the gravity field has zero mean and also that the gravity variation is harmonic, i.e. $\bar{g}_y = 0$ and

$$g_y = \cos(t + \phi) \tag{3.1}$$

where ϕ is the phase angle. These assumptions significantly reduce the number of parameters. The relevant parameters of the two-dimensional problem are then the Grashof number, $Gr = (\Delta\rho/\bar{\rho})(g/\omega^{3/2}\nu^{1/2})$; the Schmidt number, $Sc = \nu/D$; the phase angle, ϕ; the non-dimensional length of the domain, $l = L/l_v$; and the aspect ratio of the domain, $A = H/L$ where H and L are the height and length of the domain respectively. The Grashof number based on the length of the domain is $Gr_L = Grl^3$. Figure 2(*a*) shows a schematic of the simplified model problem.

When the above simplifications are taken into account, the current problem is similar to the one that has been studied by Duval & Jacqmin (1990), which provides a validation while also allowing us to pursue some issues in more detail.

https://doi.org/10.1017/S0022112006001169 Published online by Cambridge University Press

We now rewrite equations (2.4)–(2.6) taking the above simplifications into account:

$$\frac{\partial u}{\partial x} + \frac{\partial v}{\partial y} = 0, \tag{3.2}$$

$$\frac{\partial u}{\partial t} + Gr\left(u\frac{\partial u}{\partial x} + v\frac{\partial u}{\partial y}\right) = -Gr\frac{\partial p}{\partial x} + \left(\frac{\partial^2 u}{\partial x^2} + \frac{\partial^2 u}{\partial y^2}\right), \tag{3.3}$$

$$\frac{\partial v}{\partial t} + Gr\left(u\frac{\partial v}{\partial x} + v\frac{\partial v}{\partial y}\right) = -Gr\frac{\partial p}{\partial y} + \left(\frac{\partial^2 v}{\partial x^2} + \frac{\partial^2 v}{\partial y^2}\right) + \frac{\rho}{\Delta\rho}\cos(t+\phi), \tag{3.4}$$

$$\frac{\partial C}{\partial t} + Gr\left(u\frac{\partial C}{\partial x} + v\frac{\partial C}{\partial y}\right) = \frac{1}{Sc}\left(\frac{\partial^2 C}{\partial x^2} + \frac{\partial^2 C}{\partial y^2}\right). \tag{3.5}$$

In the above equations, u is the x (horizontal) component of velocity and v is the y (vertical) component of velocity.

The above equations are now recast into stream function–vorticity formulation. We introduce a stream function, ψ such that $u = \partial\psi/\partial y$ and $v = -\partial\psi/\partial x$, and $\xi = \partial v/\partial x - \partial u/\partial y$ is the out-of-plane vorticity. The equations become

$$\frac{\partial^2\psi}{\partial x^2} + \frac{\partial^2\psi}{\partial y^2} = -\xi, \tag{3.6}$$

$$\frac{\partial \xi}{\partial t} + Gr\left(u\frac{\partial \xi}{\partial x} + v\frac{\partial \xi}{\partial y}\right) = \left(\frac{\partial^2 \xi}{\partial x^2} + \frac{\partial^2 \xi}{\partial y^2}\right) + \left(\frac{\partial C}{\partial x}\right)\cos(t+\phi), \tag{3.7}$$

$$\frac{\partial C}{\partial t} + Gr\left(u\frac{\partial C}{\partial x} + v\frac{\partial C}{\partial y}\right) = \frac{1}{Sc}\left(\frac{\partial^2 C}{\partial x^2} + \frac{\partial^2 C}{\partial y^2}\right). \tag{3.8}$$

Since we have assumed that the two fluids are miscible, there is no discontinuity in the concentration at the interface ($x = 0.5l$), but since we have also assumed that the initial interface is sharp, the width of the region over which the initial concentration changes from 1 to 0 must be very small. We therefore choose the following function to represent the initial concentration field:

$$t = 0: \quad C = \tfrac{1}{2}\,\mathrm{erfc}\left(\frac{x - 0.5l}{\delta}\right). \tag{3.9}$$

Note that the above initial condition introduces an additional parameter into the problem: δ, the steepness of the initial concentration profile, which is used to eliminate discontinuities. It has been found in many similar problems that the dependence on δ is very slight.

We assume that the fluids are initially at rest. Therefore

$$t = 0: \quad \xi = 0, \quad \psi = 0. \tag{3.10}$$

The boundary conditions are as follows:

$$x = 0, l: \quad u = \frac{\partial v}{\partial x} = \frac{\partial C}{\partial x} = 0, \tag{3.11}$$

which corresponds to no fluid penetration, no shear stress, and no mass flux along the vertical walls; and

$$y = 0, lA: \quad u = v = \frac{\partial C}{\partial y} = 0, \tag{3.12}$$

https://doi.org/10.1017/S0022112006001169 Published online by Cambridge University Press

which corresponds to no fluid penetration, no slip, and no mass flux along the horizontal walls. We will be solving equations (3.6)–(3.8), subject to equations (3.9)–(3.12). Figure 2(*b*) shows a sketch of the domain along with the boundary conditions.

Consideration of the boundary conditions which specify that the stream function, vorticity and mass flux vanish along the vertical walls enables us to employ a Galerkin-type spectral discretization for the variables in the x-direction:

$$\psi(x, y, t) = \sum_k \hat{\psi}_k(y, t) \sin(k\alpha x), \tag{3.13}$$

$$\xi(x, y, t) = \sum_k \hat{\xi}_k(y, t) \sin(k\alpha x), \tag{3.14}$$

$$C(x, y, t) = \sum_k \hat{C}_k(y, t) \cos(k\alpha x). \tag{3.15}$$

In the above equations k is the wavenumber and $\alpha = 2\pi/l$. For differentiation in the y-direction we use compact finite differences (see Lele 1992) which are fourth-order accurate in the interior and third-order at the boundaries. The time integration is fully explicit and utilizes the classical fourth-order Runge–Kutta scheme. The nonlinear terms are evaluated in a pseudospectral manner. For the vorticity boundary condition along the horizontal walls, we use the standard first-order approximation (Roache 1982).

The accuracy of the results has been verified by mesh refinement. We decrease the mesh size until the results obtained with two successive mesh sizes are within 5% of each other. When the Gr and Sc are small, a grid that uses 128 modes in the horizontal direction and 256 nodes in the vertical direction was sufficient to accomplish this. However, at larger values of Gr and Sc we needed more modes and nodes.

In order to verify the accuracy of the solution we compared our results, for $\phi = 0$, with those from Duval & Jacqmin (1990) (henceforth denoted as DJ). We point out that the boundary conditions imposed on the sidewalls are different in their study: they impose a no-slip condition whereas we impose a no-stress condition. Therefore, the results are not expected to agree well at later times, when the interface interacts with the sidewalls. We choose the parameter values for case 21 in their paper: $A = 1$, $Re_s = 14.86$, $Sc = 247$, $Gr/Re^2 = 0.5888$, $Re = 637$ and $Pe_D = 1.57 \times 10^6$. We found that the concentration and stream function contours at two different times $t = \pi$ and 2π were very similar to those in figures 10(*a*) and 10(*b*) in DJ. They report that when $t = \pi$ the maximum and minimum values of the stream function in the flow domain are $\psi_{max} = 0.0257$ and $\psi_{min} = -0.0319$. When our results are suitably normalized, we observe $\psi_{max} = 0.0260$ and $\psi_{min} = -0.0332$, which is in excellent agreement. Similarly when $t = 2\pi$, DJ report that $\psi_{max} = 0.0203$ and $\psi_{min} = -0.033$. We observe that $\psi_{max} = 0.0271$ and $\psi_{min} = -0.0486$. The agreement is fair, considering that the interface was very close to the sidewalls and therefore the boundary conditions on the sidewalls became important.

4. Results

From the governing equations and the initial and boundary conditions it can be seen that the problem is governed by six parameters: the Grashof number, Gr; the Schmidt number, Sc; the phase angle, ϕ; the aspect ratio of the domain, A; the non-dimensional length of the domain, l, and the steepness of the initial concentration

https://doi.org/10.1017/S0022112006001169 Published online by Cambridge University Press

profile, δ. The reference values of these parameters are as follows. For the moment, we fix $\phi = 0$ and $Sc = 1$, which corresponds to the case of mixing of gases. We fix $A = 2$ which means that the domain is a vertical narrow cavity. l is fixed at 200 resulting in a reasonably large domain (two hundred viscous lengths, l_v) so that the evolution of the interface is free from any edge effects over a reasonably long time. δ is set at 5 resulting in a reasonably sharp but continuous interface that is easily resolvable. Gr was varied from 1 to 25 (resulting in Grashof numbers based on the length of the domain, ($Gr_L = Grl^3$) on the order of 10^8). Various quantities, especially the interfacial evolution, were studied as a function of time. Note that the results obtained for $\phi = 0$ are analogous to the results obtained for $\phi = \pi$, because $\phi = 0$ corresponds to the configuration where the heavier fluid is in the left half of the domain, whereas $\phi = \pi$ corresponds to the reverse configuration, i.e. heavier fluid is in the right half of the domain.

We observe four different flow patterns as Gr is varied. In what follows, we denote the 'interface' as the contour on which the concentration, $C = 0.5$.

4.1. *Very small Gr* ($Gr < 2$)

For small Gr inertia is very weak and the concentration field is dominated by diffusion. Even after 120 periods, we observe very little deformation of the interface. The solutions for $Gr < 2$ show that the interface simply oscillates about the vertical centreline, $x = 0.5l$. By examining the power spectrum (not shown) associated with the vertical velocity at any arbitrary point, we determine that the flow field responds at a frequency equal to that of the modulation.

4.2. *Small to intermediate Gr* ($2 \leqslant Gr < 12$)

As Gr is raised above 2, there is significant deformation of the interface and we witness the formation of a wavy structure for the interface. This structure is generated at both the top and bottom boundaries. We call these wavy structures 'folds' when their lateral extent is more than five viscous length scales. Figure 3 shows snapshots of these 'folds' for $Gr = 10$. These snapshots clearly indicate that the folds spread laterally and propagate into the fluid with time. It can also be seen that with time the number of folds also increases. The temporal evolution of the concentration field and the interface are also shown in movies 1 and 2 respectively.† To illustrate the formation of folds more clearly, in figure 4 we zoom in on a rectangular area close to the top edge of the flow domain, $90 \leqslant x \leqslant 110$ and $360 \leqslant y \leqslant 400$, (the whole flow domain extent is $0 \leqslant x \leqslant 200$ and $0 \leqslant y \leqslant 400$). The gravity vector is initially pointing upward. Therefore, in the first quarter-cycle, from $t = 0$ to $t = \frac{1}{2}\pi$, the heavier fluid, which is on the left side of the cavity, starts flowing to the right (in the top half of the cavity) and the lighter fluid flows to the left (in the bottom half of the cavity). Because of the vorticity production and the enclosure geometry a clockwise rotating flow results. Note that because we imposed a no-slip boundary condition on the top and bottom walls, the fluid does not slip along these walls but a small kink in the interface is introduced, due to diffusion in the y-direction, very near to the top and bottom walls (figure 4*b*, *c*). When $t = \frac{1}{2}\pi$, the gravity vector changes direction. However, because of inertia at finite Gr, the heavier fluid does not immediately return to its initial position but continues moving to the right (figure 4*d*, *e*). At $t = \pi$ the gravity vector is at its relative minimum. The rotation is halted and vorticity of the opposite sign is generated. So, from $t = \pi$ to $t = \frac{3}{2}\pi$, the flow field rotates in the counterclockwise

† The movies are available with the online version of the paper.

https://doi.org/10.1017/S0022112006001169 Published online by Cambridge University Press

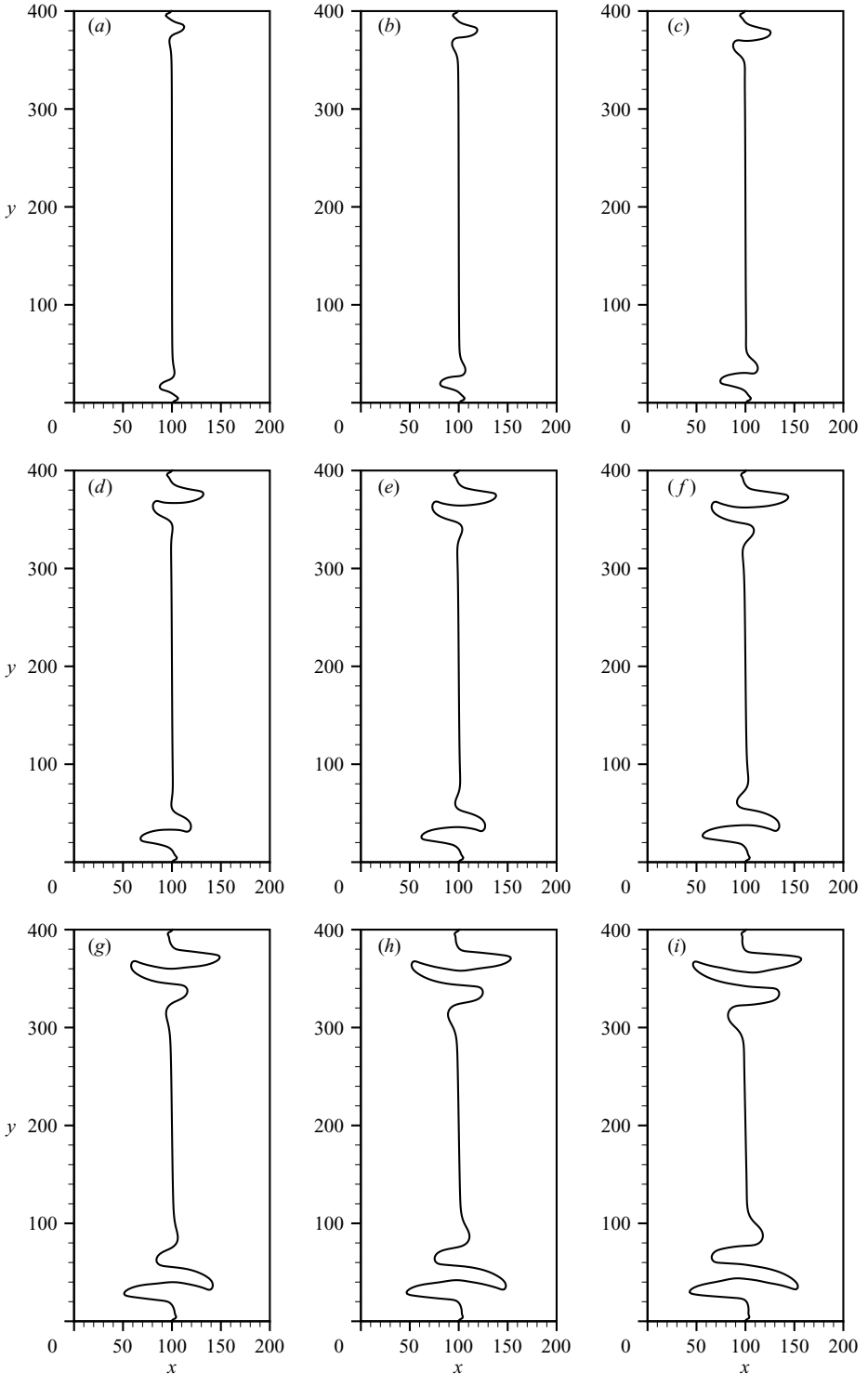

FIGURE 3. Evolution of the interface. The contour line $C = 0.5$ is shown from $t = 3\pi$ to $t = 11\pi$ in increments of π. $Gr = 10$.

https://doi.org/10.1017/S0022112006001169 Published online by Cambridge University Press

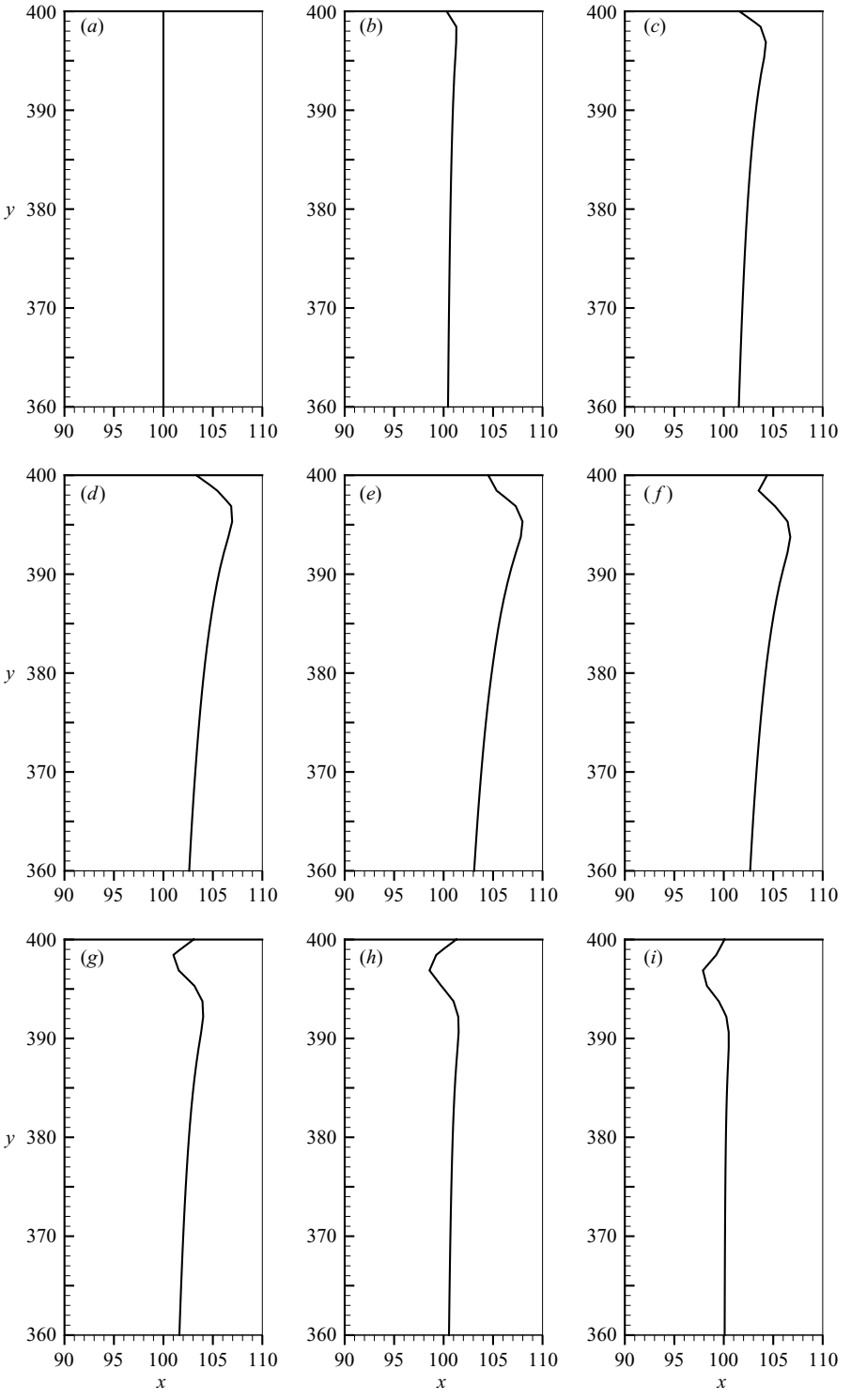

FIGURE 4. The mechanism of fold formation. The contour line $C = 0.5$ (interface) is shown from $t = 0$ to $t = 2\pi$ in increments of 0.25π. $Gr = 4$.

https://doi.org/10.1017/S0022112006001169 Published online by Cambridge University Press

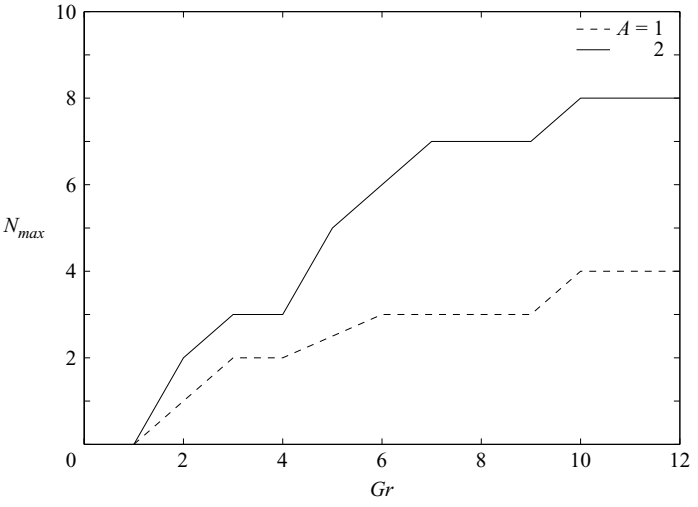

FIGURE 5. The maximum number of folds, N_{max} vs. Gr.

sense (figure 4*f*, *g*). When $t = \frac{3}{2}\pi$, the gravity vector again changes direction, but again because of inertia, the interface continues rotating in the counterclockwise sense and the heavier fluid starts moving to the left (figure 4*h*, *i*). At the end of the cycle, $t = 2\pi$ (figure 4*i*), we distinctly see the deformation of the interface and the formation of folds at the top and bottom boundaries. Thus we see that periodic production of vorticity of opposite sign, combined with finite fluid inertia, is responsible for the production of folds.

The production and propagation of folds continues until they reach the centre of the domain and begin to interact. As Gr is increased we witness an increase in the number of folds produced until this point is reached. The maximum number of folds formed, N_{max}, is shown as a function of Gr in figure 5. We count only the folds in the top half of the domain, the number of folds in the bottom half being the same. From figure 5, we also see that the maximum number of folds formed varies linearly with the aspect ratio, i.e. at any particular value of Gr, N_{max} for $A = 1$ is half of that for $A = 2$. This suggests that the average vertical propagation speed of the folds is constant at a given Gr.

Different measures are used to characterize the evolution of the interface with time. We measure their maximum lateral extent, w. We also plot the distance to which the folds propagate in the vertical direction. We define this 'propagation distance', γ as the distance (measured from the top edge) beyond which folds lie within 1% of the $x = 0.5l$ centreline. Figure 6 shows a schematic that explains how w and γ are measured. Figure 7 shows the variation in the maximum lateral extent, w, of the interface with time for different Gr. The lateral extent increases with time and, at any given time, flows with larger Gr give rise to folds with larger lateral spread. Figure 8 shows the propagation distance, γ as a function of time. The folds propagate deeper into the domain and flows with larger Gr leading to faster propagation. Note that the above results are valid only until the folds begin to interact.

It can be seen from figure 8 that there is a smooth increase in the vertical propagation distance with time followed by a rapid rise ('jump') and this cycle repeats itself. The typical variation of the vertical propagation distance in between jumps is

https://doi.org/10.1017/S0022112006001169 Published online by Cambridge University Press

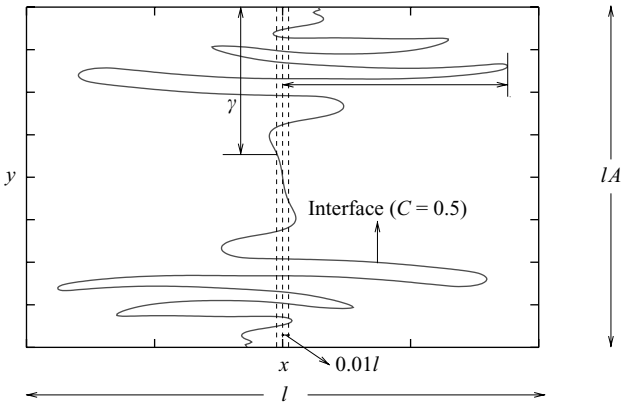

FIGURE 6. Schematic explaining the measurement of γ and w.

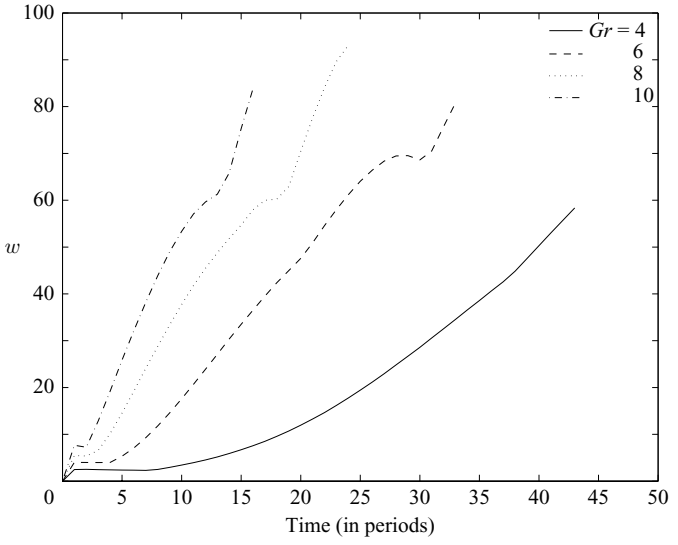

FIGURE 7. Growth of maximum lateral extent, w with time, t.

plotted in figure 9. A square-root fit approximates this variation of γ very well, which suggests that the propagation of folds is due to diffusion.

It has also been observed that, for small times, the entire mechanism of fold production and propagation is self-similar for $4 \leqslant Gr \leqslant 9$. This can be observed by suitably normalizing the vertical propagation distance, γ, and time, t, using powers of Gr. The functions of Gr that are used to normalized γ and t are chosen such that the normalized values at which we observe the first jump (in normalized γ) is the same for all Gr (although other methods of scaling give similar results). A graph illustrating this self-similarity is plotted in figure 10, and can be expressed mathematically as

$$\gamma Gr^{0.53} = f(tGr^{1.71}), \tag{4.1}$$

Equation (4.1), although a fit to the data, can be further manipulated to give insight into the mechanisms involved. Adopting the values of 1/2 and 5/3 for the exponents, and using the fact from figure 9 that the function f is quadratic in its argument, we

https://doi.org/10.1017/S0022112006001169 Published online by Cambridge University Press

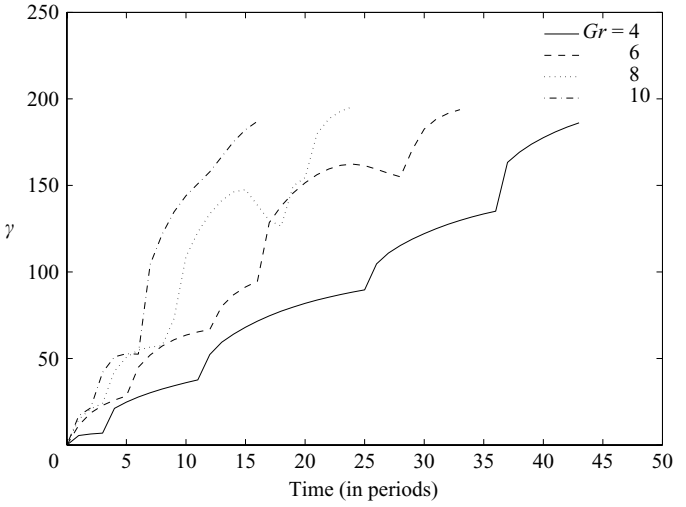

FIGURE 8. Growth of vertical propagation distance, γ with time, t.

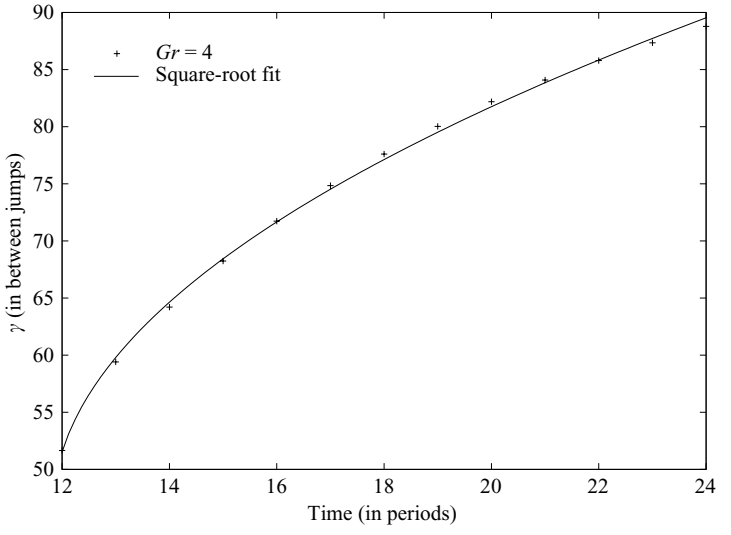

FIGURE 9. Square-root variation of the vertical propagation distance, γ, in between jumps. $\gamma(t) = 10.99\sqrt{1.26t - 14.95} + 46.44$.

find for the dimensional propagation distance of a fold,

$$\gamma' \sim \sqrt{\nu t}\, Gr^{1/3}. \tag{4.2}$$

Thus, the folds propagate diffusively, but with a rate that is amplified by the flow. The exponent of 1/3 is suggestive of a Leveque-like convection–diffusion balance in which vorticity is produced at the ends of the folds ($\partial C/\partial x$ is non-zero there), and is then convected to one side or the other by the nearly parallel shear flow between them. The process is loosely analogous to the production and propagation of vorticity in a Stokes layer, but with important differences. In the Stokes layer, vorticity transport is entirely diffusive and vorticity of opposite sign is produced over each half-period of the oscillation at the boundaries. In the present problem, vorticity is transported

https://doi.org/10.1017/S0022112006001169 Published online by Cambridge University Press

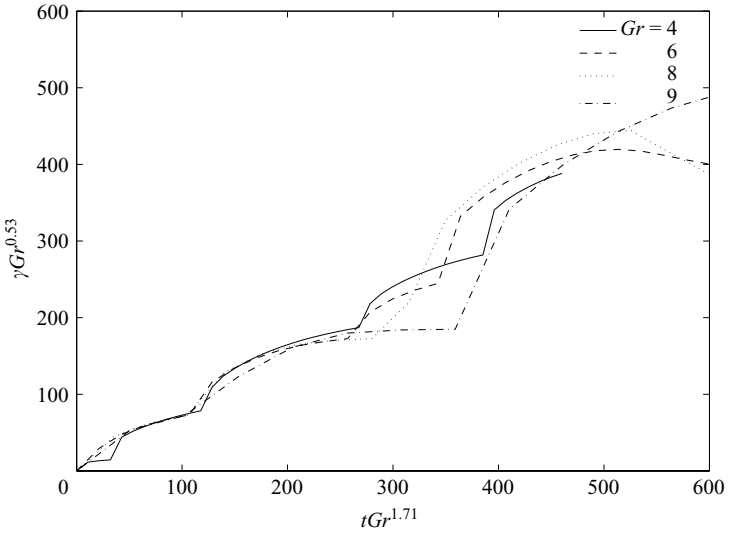

FIGURE 10. Self-similarity of the folds for $4 \leqslant Gr \leqslant 9$.

by both convection and diffusion and the vorticity production, while still of opposite sign over each half-period, is distributed throughout the fluid.

4.3. *Intermediate to large Gr* ($12 \leqslant Gr < 18$)

As we mentioned earlier, there is a nearly parallel shear flow between the folds. From figure 7, we see that the width of the folds increases with Gr, which means that the strength of the parallel shear flow increases with Gr. As Gr increases, inertia increases, resulting in an increased potential for inertial modes, and diffusion decreases, weakening the stabilizing mechanism. Thus, at moderate to large Gr, there is a potential for shear instabilities, such as those observed in free shear layers and in gravity currents with steady gravity, e.g. Simpson (1969). For $12 \leqslant Gr < 18$, we observe a new regime of behaviour, wherein we observe that corrugations start to develop on the folds. These wrinkles grow in size and eventually *small concentration pockets become detached* from the interface and propagate into the flow field. The propagation of these waves is mainly in the horizontal direction, and the disturbances are similar in appearance to the Kelvin–Helmholtz billows which have been observed in gravity currents with steady gravity and, more generally, in free shear layers. Waves associated with Kelvin–Helmholtz instability have also been observed in Duval & Jacqmin (1990). Figure 11, wherein we plot only the concentration contours for $C = 0.25$ to $C = 0.75$ for clarity, illustrates this behaviour. The detachment of the concentration pockets can be seen in panels (e–g) between $x \sim 150$ and 200 and $y \sim 50$ and 100. In order to show the corrugations on the folds more clearly, we have zoomed in figure 12 on a rectangular region with coordinates $0 \leqslant x \leqslant 200$ and $50 \leqslant y \leqslant 100$. The detachment of the concentration pockets from the interface can be seen in figure 12d, e between $x \sim 150$–200 and $y \sim 60$–80. Movies 3 and 4 illustrate the occurrence of Kelvin–Helmholtz instability on the folds and the resulting detachment of the concentration pockets.

4.4. *Large Gr* ($Gr \geqslant 18$)

Owing to the formation of folds, there are some regions in the domain where the net acceleration is directed from the lighter fluid towards the heavy fluid, creating

https://doi.org/10.1017/S0022112006001169 Published online by Cambridge University Press

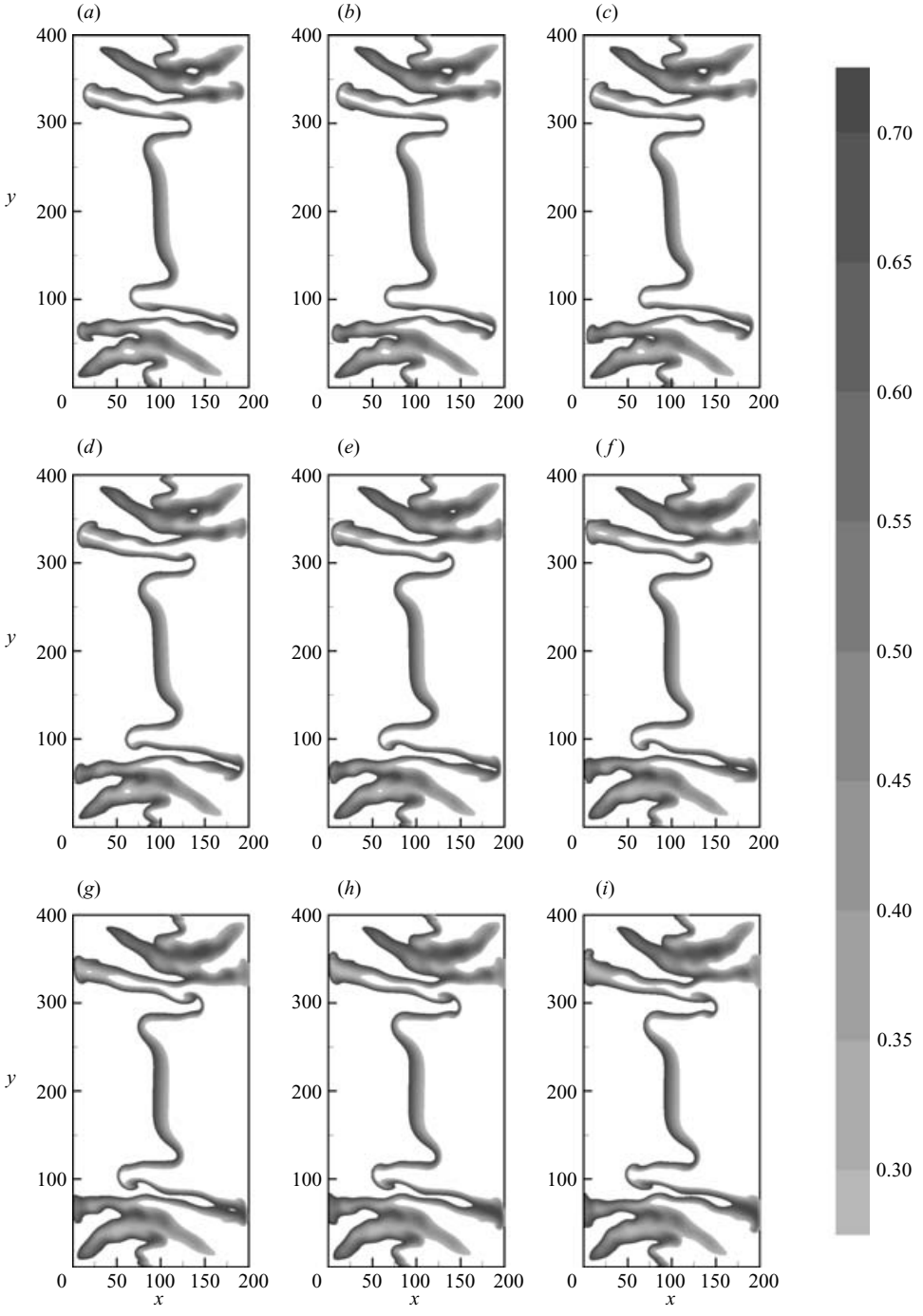

FIGURE 11. The detachment of concentration pockets from the interface due to Kelvin–Helmholtz instability. $t = 21.5\pi$–23.5π in increments of 0.25π, $Gr = 14$.

the potential for Rayleigh–Taylor instability. Also, an increasing Gr corresponds to larger density difference, higher acceleration, sharper density gradients, or all three. Thus, there is an increased potential for Rayleigh–Taylor instability for larger Gr. For $Gr \geqslant 18$, we observe another new regime of behaviour, in which we observe both

https://doi.org/10.1017/S0022112006001169 Published online by Cambridge University Press

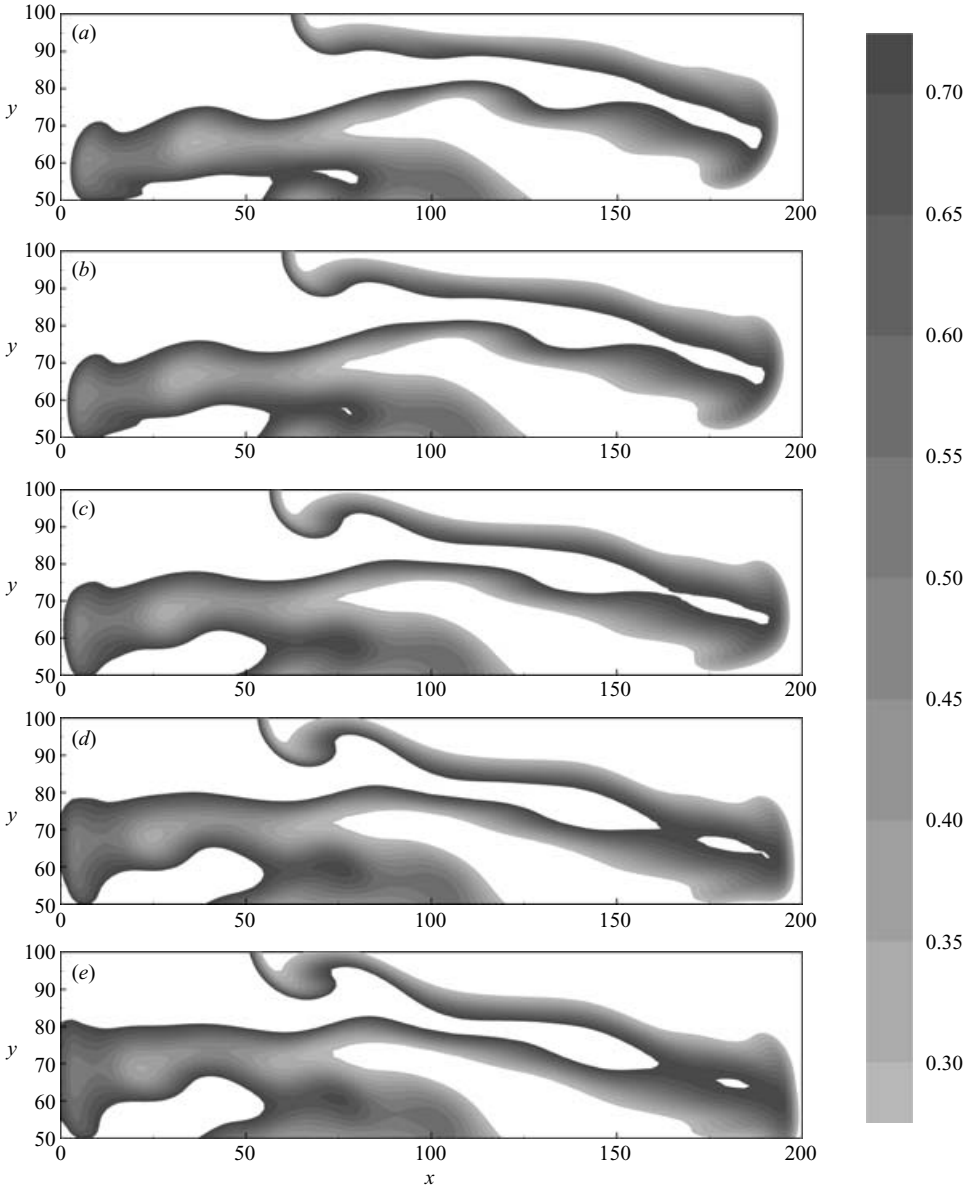

FIGURE 12. The detachment of concentration pockets from the interface due to Kelvin–Helmholtz instability. $t = 22\pi$–23π in increments of 0.25π, $Gr = 14$.

Kelvin–Helmholtz billows and another kind of instability which propagates mainly in the vertical direction. The snapshots of the concentration field shown in figure 13 reveal the deformation of the interface into a mushroom structure with the interface rolling up into counter-rotating vortices, which is commonly observed when there is Rayleigh–Taylor instability (see Sharp 1984; Tryggvason 1988). Tryggvason (1988) did extensive numerical investigations of the Rayleigh–Taylor instability and found that when the density difference is small the interface rolls up into two counter-rotating vortices and when the density difference is large there is no vortex roll-up and a 'bubble-spike' pattern is observed instead. In our study, since the density

https://doi.org/10.1017/S0022112006001169 Published online by Cambridge University Press

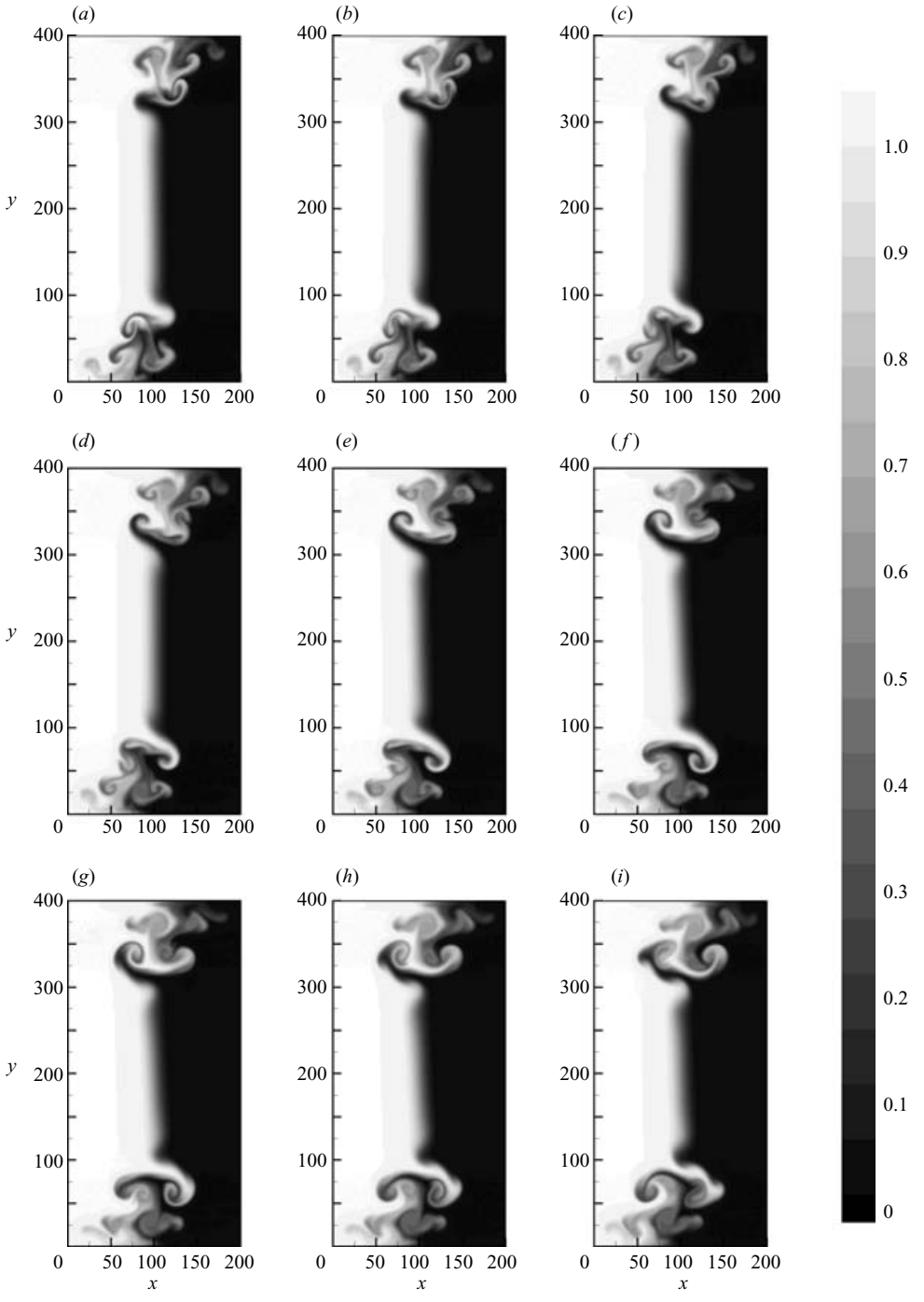

FIGURE 13. The Rayleigh–Taylor instability. Concentration field for $t = 8.5\pi$–10.5π in increments of 0.25π, $Gr = 22$.

difference is small, we also observe a mushroom structure with two counter-rotating vortices. This structure can be seen in figure 13(*e–i*) between $x \sim 50$–150 and $y \sim 300$–350. Movie 5 also illustrates the occurrence of these Rayleigh–Taylor mushrooms.

https://doi.org/10.1017/S0022112006001169 Published online by Cambridge University Press

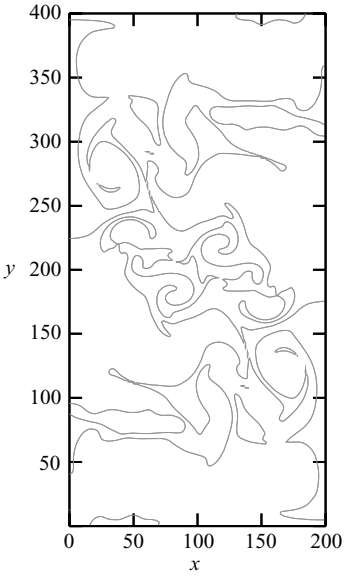

FIGURE 14. The highly disordered interface at $t = 30\pi$ for $Gr = 22$.

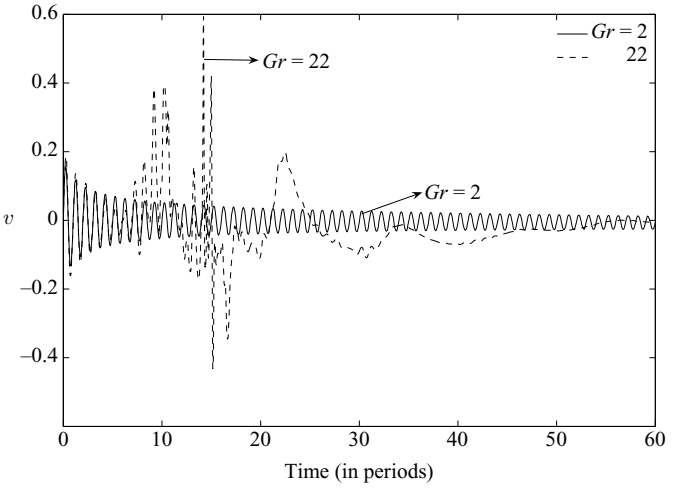

FIGURE 15. The variation of vertical velocity, v, with t for $Gr = 2,\ 22$ at $x = 98.4375,\ y = 218.75$.

Figure 14 presents snapshots of the interface at a later time, $t = 30\pi$. We see that the concentration field is very disordered, leading to neither organized Kelvin–Helmholtz rollers nor Rayleigh–Taylor mushrooms. This disordered concentration field suggests the possibility of chaotic flow, as a result of these instability modes, which we investigated by considering the dynamics of point quantities.

4.5. *Dynamics of point quantities*

In figure 15 we show the variation of the vertical velocity, v, measured at the point, $(x,\ y) = (98.4375,\ 218.75)$, with time, t, for two different Grashof numbers, $Gr = 2,\ 22$. This particular point was chosen because we expect the flow behaviour

https://doi.org/10.1017/S0022112006001169 Published online by Cambridge University Press

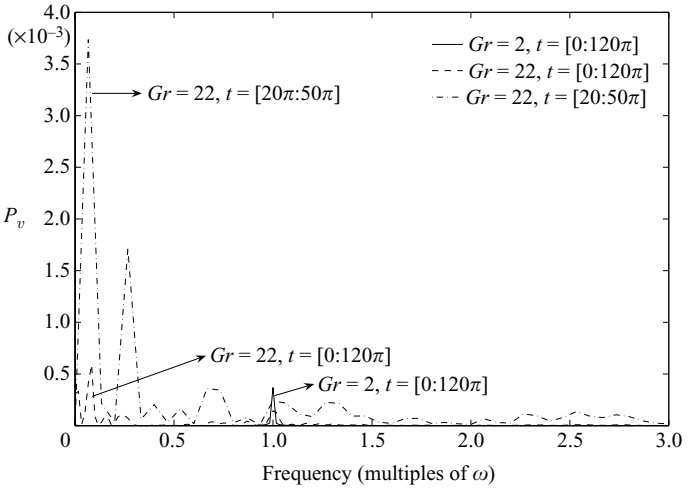

FIGURE 16. The power spectra of the vertical velocity, v, for $Gr = 2,\ 22$ at $x = 98.4375,\ y = 218.75$.

to be complex at points which are either on or very close to the interface ($x = 100$) between the fluids. For $Gr = 2$, the variation of v with t is harmonic, while for $Gr = 22$, the variation is periodic for small times ($t \leqslant 20\pi$), but for later times ($20\pi < t \leqslant 50\pi$) it is aperiodic accompanied by large fluctuations, and at even later times ($t > 50\pi$), the velocity decays to zero. In figure 16 we plot the power spectra of v. For $Gr = 2$ the spectrum is just a single spike at the forcing frequency. For $Gr = 22$ we compute the power spectra over two time spans: $t = [0 : 120\pi]$, which corresponds to the entire time span, and $t = [20\pi : 50\pi]$, which corresponds to the time over which the velocity variation is aperiodic accompanied by large fluctuations. The motivation for computing the power spectrum over $t = [20\pi : 50\pi]$ is that this is the time span over which mixing is the most vigorous. Thus we expect the power spectrum over this time span to have contributions from a range of frequencies. It can be seen that the power spectra for $Gr = 22$, over both time spans, while certainly rich, are not broadband. This suggests that the flow field is not chaotic at $x = 98.4375,\ y = 375$. We have also experimented with some other points in the flow field and we could not find any point where the power spectrum was broadband. We have also experimented with other flow quantities (horizontal velocity, vorticity, stream function, etc.) and have observed that they all show the same general trend: harmonic variation for very small Gr and aperiodic variation for large Gr. Thus we conclude that while the flow field is certainly disordered at some points, it is not chaotic, over the range of parameters covered here.

We have repeated the above analysis for points that are far from the interface and found that for both $Gr = 2$ and 22, the flow field responds at the forcing frequency. Thus the flow field is disordered only at points that are either on or close to the interface.

4.6. *Effect of Sc*

As we have seen, as Gr is increased we observe first Kelvin–Helmholtz instability and then Rayleigh–Taylor instability. We varied Sc from 1 to 100 and observed the transitions in order to find out if the Rayleigh number, $Ra = GrSc$, is the more relevant stability parameter. We determined the critical Grashof numbers at which we first

https://doi.org/10.1017/S0022112006001169 Published online by Cambridge University Press

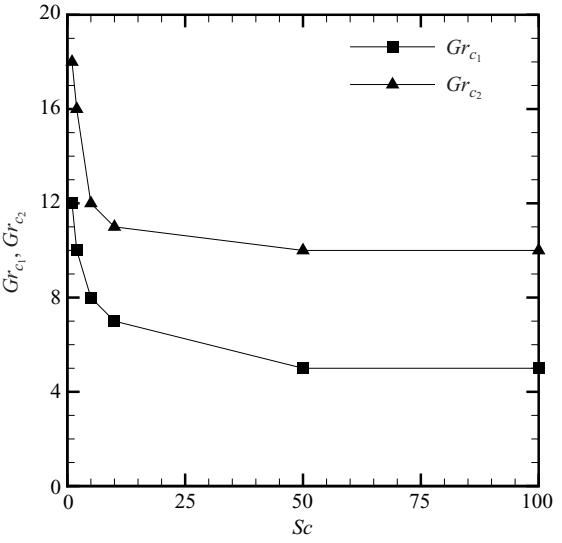

FIGURE 17. The variation of the critical Gr at which Kelvin–Helmholtz and Rayleigh–Taylor instabilities first appear, Gr_{c_1}, Gr_{c_2} respectively, with Sc.

observe Kelvin–Helmholtz instability, Gr_{c_1} and that for Rayleigh–Taylor instability, Gr_{c_2} as functions of Sc. In figure 17 we plot Gr_{c_1} and Gr_{c_2} *vs.* Sc, from which it can be seen that the critical Grashof numbers become independent of Sc for moderately large Sc, suggesting that for the present problem, Ra is not a more relevant parameter than Gr, and that the mechanisms for exciting the Kelvin–Helmholtz and Rayleigh–Taylor instabilities are inertial in nature. As Sc decreases, the interface becomes more diffuse, leading to some degree of stabilization (larger Gr_c) relative to the sharp interface case.

4.7. *Effect of l*

The motivation for varying l is to understand the effect of varying the frequency of the modulation, ω, on the evolution of the interface. ω appears in two parameters: the Grashof number, $Gr = (\Delta\rho/\bar{\rho})(g/\omega^{3/2}\nu^{1/2})$ and the non-dimensional domain size, $l = L/\delta_\nu = L\sqrt{\omega}/\sqrt{\nu}$. The following combination of the above two parameters,

$$Gr_L = Grl^3 = \frac{\Delta\rho}{\bar{\rho}} g \frac{L^3}{\nu^2},$$

which represents the Grashof number based on the length of the domain, does not contain ω. In order to investigate the effect of varying ω, we keep Gr_L constant at a representative value, 8×10^6, and vary l. For $l = 200$, which corresponds to $Gr = 1$, we see from figure 18(a) that there are no interfacial folds. When l is reduced to 100, which corresponds to $Gr = 8$ and to reducing the frequency by a factor of 4, we observe the formation of folds on the interface, as seen in figure 18(b). When l is further reduced to 73.6681, which corresponds to $Gr = 20$ and to reducing the orginal frequency by a factor of 7.368, we observe the occurrence of Rayleigh–Taylor instability, as can be seen from the mushroom structures at the top-left and bottom-right corners of figure 18(c). Thus we see that reducing the frequency, while keeping all the other parameters except Gr constant, makes the concentration field more disordered.

https://doi.org/10.1017/S0022112006001169 Published online by Cambridge University Press

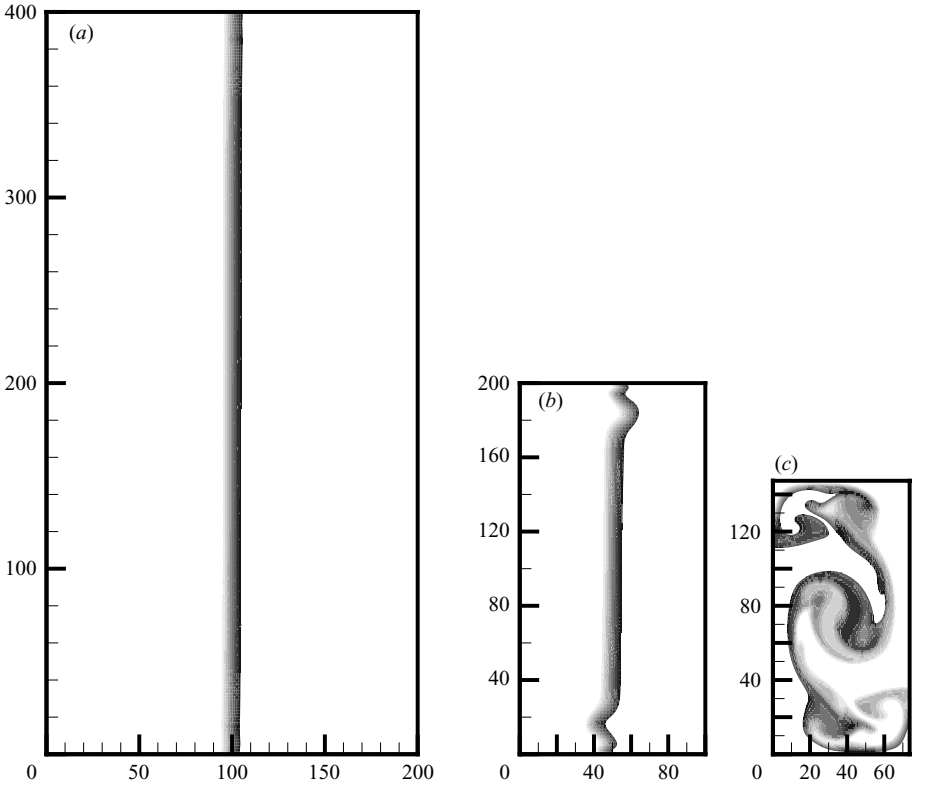

FIGURE 18. The effect of frequency. (*a*) $Gr = 1$, $a = 200$, $t = 3.25$ periods – no folds; (*b*) $Gr = 8$, $a = 100$, $t = 3.25$ periods – interfacial folds; (*c*) $Gr = 20$, $a = 73.681$, $t = 3.25$ periods – Rayleigh–Taylor instability.

It must be noted that in our analysis, the non-dimensional length of the domain, l, is typically large, of the order of 100, so that the evolution of the interface, which is our primary interest, is free from any edge effects over reasonably large times. When we decrease l, keeping all other parameters including Gr constant, which corresponds to reducing the dimensional geometric length L of the cavity, we expect the effects of viscous diffusion to increase.

4.8. *Effect of A*

We conducted a few studies in order to determine the effect of aspect ratio. We chose three different aspect ratios, $A = 0.5,\ 1.0,\ 2.0$ which correspond to wide, square, and narrow cavities respectively. As we pointed out earlier, the number of folds formed decreases as the aspect ratio is decreased. Since Kelvin–Helmholtz and Rayleigh–Taylor instabilities occurring on the interfacial folds are responsible for making the flow field disordered we expect that the flow field will be less disordered for low A, which in turn suggests that the mixing will be reduced for low A. Figure 19 shows the fractional mixing volume, V_m, defined as the fraction of the total volume wherein the concentration values lie between 0.45 and 0.55. As A is decreased the fractional mixing volume is decreased, which means that mixing is suppressed. We have also investigated the effect of A on Gr_c and observed that Gr_{c_1} and Gr_{c_2} are independent of A, which is consistent with our conclusion that the mechanisms for the Kelvin–Helmholtz and Rayleigh–Taylor instabilities are local.

https://doi.org/10.1017/S0022112006001169 Published online by Cambridge University Press

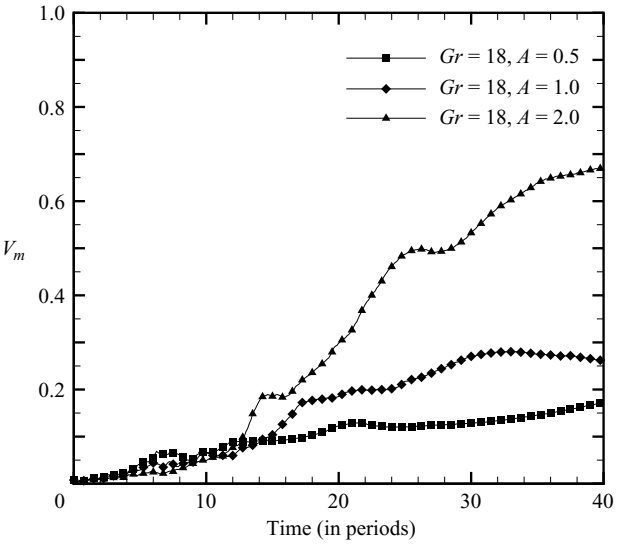

FIGURE 19. The variation of the fractional mixing volume, V_m vs. A.

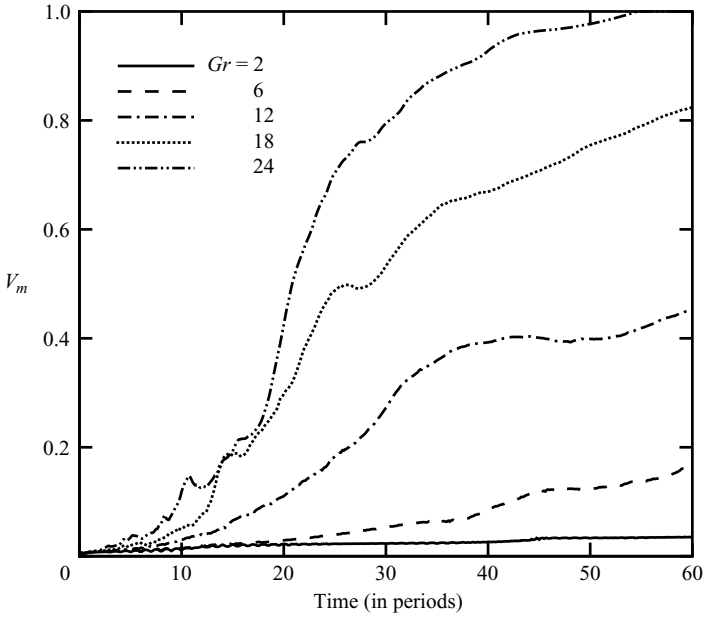

FIGURE 20. The variation of the mixing volume, V_m with time for different Gr.

4.9. *Mixing*

We adopt two measures to quantify mixing: the fractional mixing volume defined in the previous subsection and the length stretch of a material line which is initially coincident with the interface between the fluids.

In figure 20 we plot the variation of the fractional mixing volume, V_m, defined in the previous subsection, with time for different values of Gr. It can be seen that the mixing volume increases with time and also that, in general, it increases with

https://doi.org/10.1017/S0022112006001169 Published online by Cambridge University Press

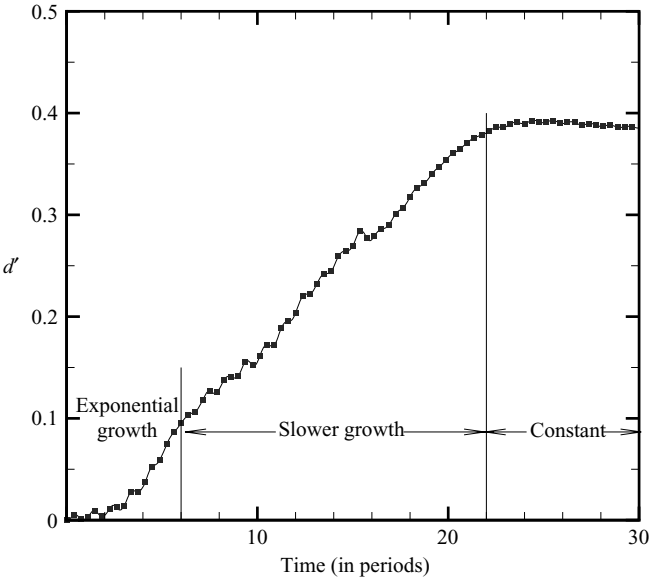

FIGURE 21. The typical variation of the line stretch with time, $Gr = 18$, $A = 1$.

increasing Gr. This is consistent with our observation that as Gr is increased the flow field becomes more disordered thus resulting in better mixing.

Mixing involves stretching and folding of material elements (see Ottino 1989, p. 64). Thus computing the stretch of a material line is useful in characterizing the effectiveness of the flow field in causing mixing. The material line stretch is defined as $d' = (d - d_0)/d_0$, where d_0 is the initial length of the material line and d is the length of the material line at time t. We consider a material line initially coincident with the interface, therefore d_0 is equal to the height of the domain, $d_0 = lA$. We mention that this material line stretch is different from the interfacial length stretch which is measured in Duval (1992). As mentioned in Ottino (1982), material lines and surfaces do not break or change topology. In contrast, the interface, which has been previously defined as the iso-concentration line ($C = 0.5$), may break up as illustrated in figures 12 and 14. Thus, the material line stretch and the interfacial length stretch are two different quantities.

In what follows, we briefly describe the algorithm used to compute the material line stretch. The material line is initially populated by N uniformly spaced passive particles. These particles are advected using the equations $\mathrm{d}x_p/\mathrm{d}t = u_p$ and $\mathrm{d}y_p/\mathrm{d}t = v_p$ where (x_p, y_p) are the spatial coordinates of particle p and (u_p, v_p) are the flow velocity components at (x_p, y_p). These velocities are obtained by linear interpolation of the flow velocities at the nodes and the particle positions are advanced in time using the classical fourth-order Runge–Kutta method. The material line is approximated as the sum of straight lines between two adjacent particles. As the material line stretches and folds, we may need to increase the number of particles in order to represent the material line accurately. However, for the range of parameters and times that are considered in this paper, $N = 10000$ particles seem more than sufficient to accurately describe the evolution of the material line.

In figure 21 we show a typical line stretch with time. For small times, there is a very rapid increase in the length of the material line. With time, the rate of increase of the length slows down and eventually the length of the material line becomes constant.

https://doi.org/10.1017/S0022112006001169 Published online by Cambridge University Press

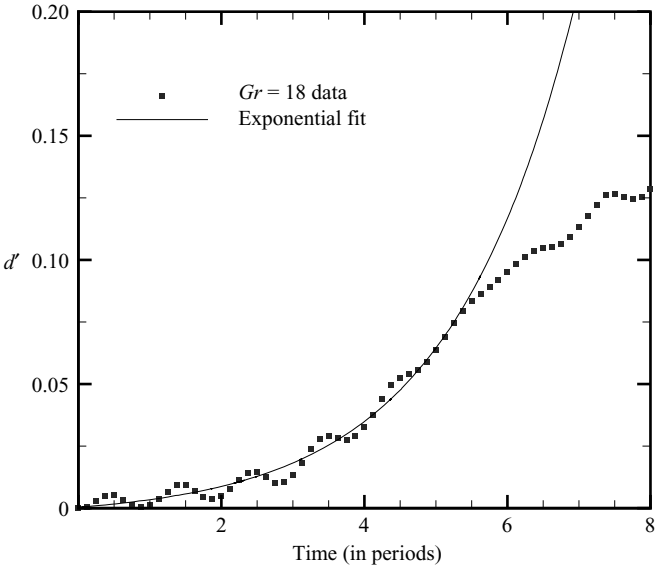

FIGURE 22. Exponential fit for the line stretch for $t \leqslant 11\pi$ for $Gr = 18$. $d' = m\exp(b\,t) + n$ with $m = 0.003936$, $b = 0.570091$, and $n = -0.003553$.

The reason for this behaviour is explained as follows. The interaction between the concentration gradients and gravity is the driving force behind the flow. Thus for small times the stretch rate is very rapid because the initial concentration gradients are large and with time, as the fluids mix, the concentration gradients decrease in magnitude, the velocities diminish, as does the stretch rate. Eventually, as the fluids become well-mixed, the concentration in the entire domain is the same ($C = 0.5$). Therefore, there is no concentration gradient and hence no flow. Thus we expect the length of the material line to increase very rapidly for small times and with time the rate of stretch slows down and eventually goes to zero. For small times, the rapid increase in the length of the line is represented well by an exponential fit, $d' = m\exp(b\,t) + n$ shown in figure 22. In figure 23 we plot the exponents b, obtained from the exponential fit, as a function of Gr. It can also be seen that for small to moderate Gr, the exponents are almost constant and for moderate to large Gr, the exponents increase with Gr. In figure 24 we show the variation of line stretch with time for various Gr. For small times, the line stretch increases with Gr. At later times, the line stretch for a flow with low Gr may be higher than that for a flow with higher Gr. The reason for this is explained as follows. A flow with higher Gr is more disordered than one with a lower Gr, thus the rate of mixing is initially higher. Therefore, the fluids become well-mixed faster and the line stretch becomes constant sooner for a flow with high Gr. At later times, the concentration gradients are higher for a flow with a lower Gr and hence the stretch of the material line is larger.

5. Effect of phase angle, ϕ

The gravity modulation is of the form $\cos(t + \phi)$. When $\phi = 0$, gravity is initially positive and after a time $t = \frac{1}{2}\pi$, it becomes negative. In contrast, when $\phi = \frac{1}{2}\pi$, gravity is negative over the times $0 < t < \pi$ and after a time $t = \pi$, it reverses its sign. Thus, changing the phase angle changes the time over which the first sign reversal of gravity occurs. Of course, changing the phase angle affects only the time of the

https://doi.org/10.1017/S0022112006001169 Published online by Cambridge University Press

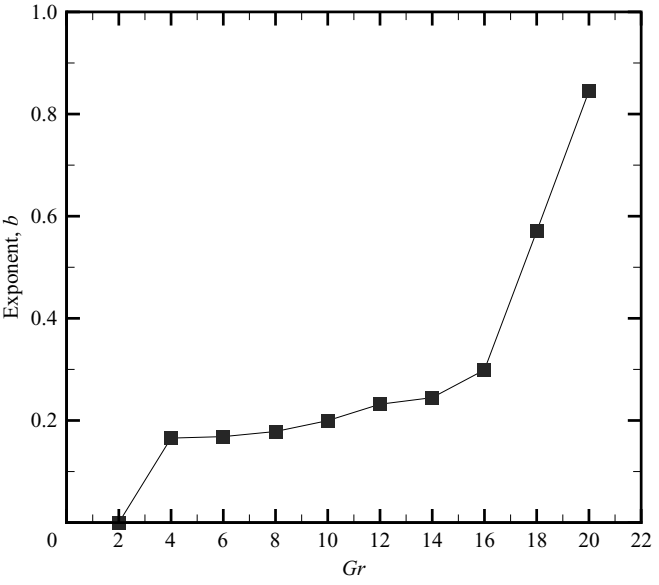

FIGURE 23. The variation of the exponents b, obtained from the exponential fit, with Gr.

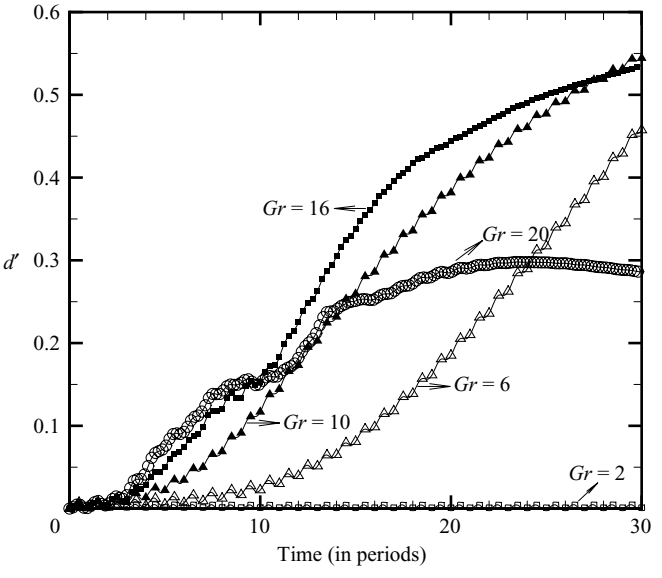

FIGURE 24. The variation of the line stretch with time for different Gr.

first sign reversal; later sign reversal periods are π for all ϕ. We expect this first sign reversal time to affect the flow and concentration fields because of finite fluid inertia. Investigating this effect is the motivation for varying the phase angle, ϕ. It should also be noted that the maximum first sign reversal time is π, which occurs for $\phi = \frac{1}{2}\pi$ and $\frac{3}{2}\pi$. We therefore expect the effect of the phase angle to be maximum for these two values.

When the phase angle of the gravity modulation, $\phi \neq 0, \pi$, the resulting flow initially closely resembles a lock-exchange flow (see Simpson 1969). For the moment we set $Sc = 1$ and $\delta = 5$. We fix the aspect ratio of the domain, $A = \frac{1}{5}$ and the length of

https://doi.org/10.1017/S0022112006001169 Published online by Cambridge University Press

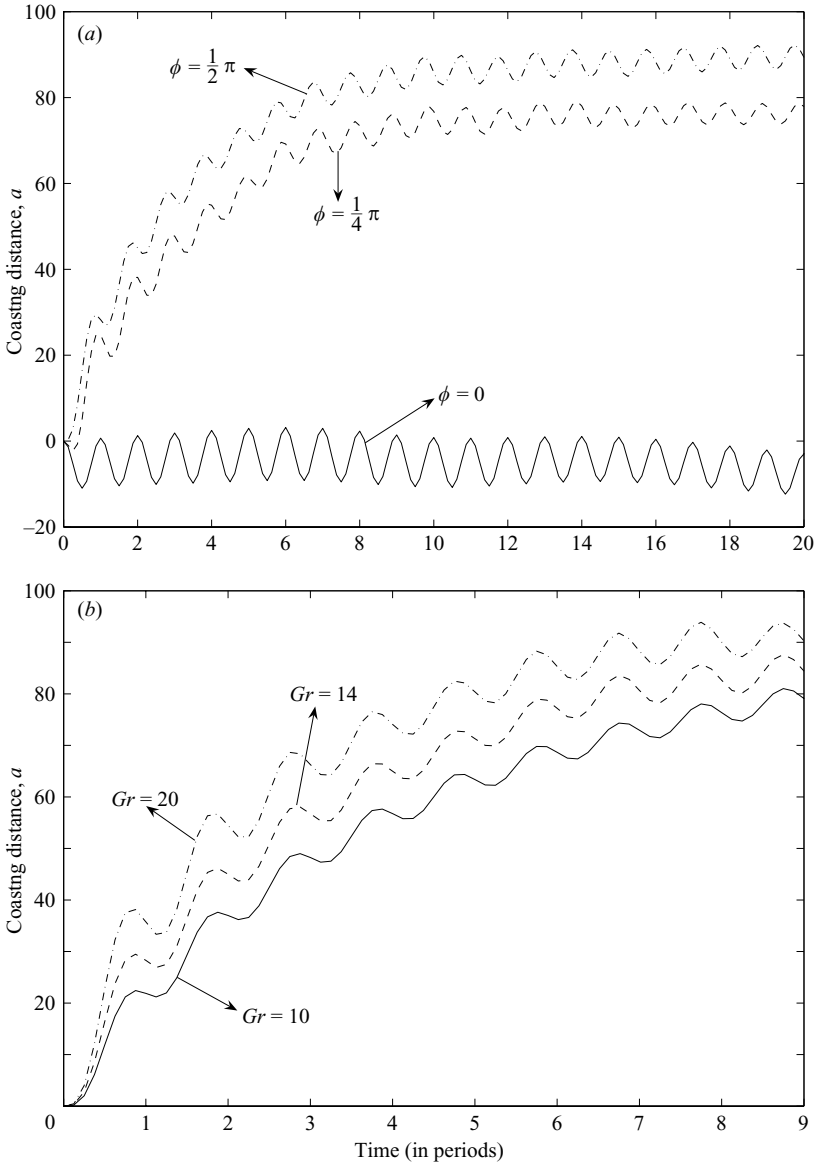

FIGURE 25. The movement of the interface along the bottom wall when $A = \frac{1}{10}$: (*a*) a vs. t for $\phi = 0, \frac{1}{4}\pi, \frac{1}{2}\pi$ when $Gr = 14$; (*b*) a vs. t for $Gr = 10, 14, 20$ when $\phi = \frac{1}{2}\pi$.

the domain, $l = 1000$. The reason for this rather large domain length is explained in the next paragraph. Unless otherwise specified, the phase angle of the modulation, $\phi = \frac{1}{2}\pi$. We have also experimented with other values of $\phi = \frac{1}{4}\pi, \frac{3}{4}\pi, \ldots$ and found that the flow regimes are the same as those when $\phi = \frac{1}{2}\pi$.

When $\phi = 0$, it was observed that the interface oscillates about the vertical centreline of the domain, i.e. the net displacement of the interface along the top (and bottom) wall after each time period is very small (figure 3). However, when $\phi = \frac{1}{2}\pi$, a gravity current is formed because of finite fluid inertia and there is significant movement of the interface along the top and bottom walls. We refer to this displacement (measured from the centreline) as the 'coasting distance', a. Figure 25(*a*) illustrates

https://doi.org/10.1017/S0022112006001169 Published online by Cambridge University Press

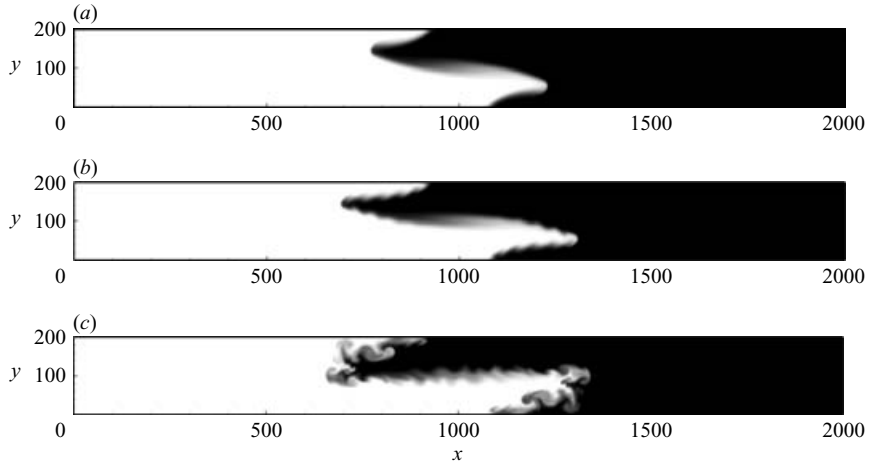

FIGURE 26. The concentration fields for (*a*) $Gr = 10$, (*b*) $Gr = 14$, and (*c*) $Gr = 20$ when $t = 10$ periods. $\phi = \frac{1}{2}\pi$.

this movement for the cases when $\phi = 0$, $\frac{1}{4}\pi$, and $\frac{1}{2}\pi$. It can be seen that for non-zero ϕ, the coasting distance increases with time and eventually becomes constant. The following expression was found to fit the data well:

$$a = \alpha e^{-\zeta t} + a_\infty + \kappa \cos(t). \tag{5.1}$$

This expression suggests that after initial transients, the interface on the top and bottom walls oscillates about the final coasting distance, a_∞, with a small amplitude κ ($\kappa \ll a_\infty$); a_∞ increases with ϕ and as expected is maximum for $\frac{1}{2}\pi$. It can be quite large, of the order of 100 viscous lengths, necessitating a large l. From figure 25(*b*) we see that both a_∞ and κ increase with Gr, because of the increase in inertia.

The inertial movement of the interface results in a significant change in the concentration profiles and we investigate if there are any changes in the flow regimes. As Gr is increased we observe the following progression of flow regimes: smooth propagation of the gravity current (figure 26*a*); localized shear instabilities (figure 26*b*); and localized shear and convective instabilities (figure 26*c*). The critical Gr for the onset of the Kelvin–Helmholtz and Rayleigh–Taylor instabilities, Gr_{c_1} and Gr_{c_2} respectively, are unchanged by the variation in ϕ. The different flow regimes with increasing Gr can also be seen in movie 6.

The motivation for phase averaging is to investigate what happens when the gravity modulation involves more than one phase. Phase averaging in the case of harmonic modulation is analogous to ensemble averaging for stochastic modulation, the effects of which will be investigated in a future paper. The phase-averaged concentration fields are obtained by averaging the concentration fields corresponding to various phase angles from 0 to 2π, in increments of $\frac{1}{8}\pi$. In figure 27 we present the phase-averaged concentration fields for $Gr = 10$ and 14 at $t = 30\pi$. We present only the concentration contours from 0.25 to 0.75. We observe the formation of a banded structure which spreads dispersively. This banded structure can be explained as follows. When the phase angle is between 0 and $\frac{1}{2}\pi$ or between $\frac{3}{2}\pi$ and 2π, gravity is initially positive and the interface initially coasts to the left in the bottom half of the domain. However, when the the phase angle is between $\frac{1}{2}\pi$ and $\frac{3}{2}\pi$, gravity is initially negative and the interface initially coasts to the right in the bottom half of

https://doi.org/10.1017/S0022112006001169 Published online by Cambridge University Press

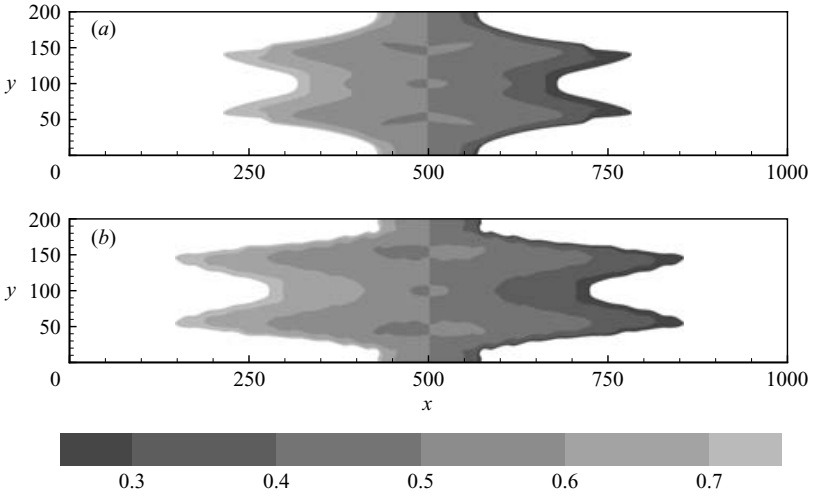

FIGURE 27. The phase-averaged concentration field for (*a*) $Gr = 10$, $A = \frac{1}{5}$ and (*b*) $Gr = 14$, $A = \frac{1}{5}$ at $t = 30\pi$.

the domain. Thus when we average over all the phase angles from 0 to 2π, we get a banded structure in the centre of the domain, which is composed of the individual interfaces, corresponding to the different ϕ between 0 and 2π. Since the individual interfaces move at different speeds as suggested by figure 25(*a*), the spread of the banded structure is dispersive. The outer limits of this banded structure are determined by the positions of the deformed interface when $\phi = \frac{1}{2}\pi$ and $\frac{3}{2}\pi$. The spread of this banded structure is larger for $Gr = 14$ because of the increased inertia compared to when $Gr = 10$. The phase-averaged concentration fields are also presented in movie 7.

6. Summary

We have investigated the physical mechanisms by which harmonic gravity modulation affects the mixing of two miscible fluids which are initially separated by a thin vertical diffusion layer. The Boussinesq approximation was invoked and the resulting equations were solved numerically and the evolution of the flow field was observed. The problem was found to be governed by six parameters: the Grashof number, Gr; the Schmidt number, Sc; the aspect ratio of the domain, A; the non-dimensional length of the domain, l; the phase angle of the gravity modulation, ϕ; and the steepness of the initial concentration profile, δ.

When $\phi = 0, \pi$, as Gr is varied we observe four different flow regimes. For very small Gr, we find neutral oscillations of the interface at the forcing frequency. For small to moderate Gr, we observe that folds start to form on the interface and the propagation of these folds is found to be self-similar and due to diffusion. For moderate to high Gr, we observe localized Kelvin–Helmholtz instability on the folds which results in the detachment of small concentration pockets from the interface. When Gr is high we observe both Kelvin–Helmholtz and Rayleigh–Taylor instabilities leading to a highly disordered flow field. An investigation of the dynamics of point quantities suggested that even though the flow is disordered, it is not chaotic. The length stretch of a material line initially coincident with the interface is found to be exponential for small times. It is also observed that larger Gr lead to increased fluid mixing. By varying

https://doi.org/10.1017/S0022112006001169 Published online by Cambridge University Press

Sc, we found that *Gr* is indeed the relevant stability parameter and that the driving mechanism for these instabilities is inertial in nature. By varying the non-dimensional length l, while keeping Grl^3 constant, we found that low-frequency modulation leads to a more disordered concentration field. The flow field is found to be less disordered for low A which explains the low mixing.

When $\phi \neq 0$ or π, the flow is similar to a lock-exchange flow, which is observed in the context of gravity currents with steady gravity. We observe three different flow regimes as *Gr* is varied: smooth propagation of the gravity current; localized shear instabilities; and localized shear and convective instabilities. Phase-averaged concentration field shows the formation of a banded structure which spreads dispersively, and whose spread increases with *Gr*, due to the increased inertia.

It now remains to compare our results for $\phi = 0$ with those of Duval & Jacqmin (1990), who studied a similar problem, but with different boundary conditions. In both our study and theirs, the basic flow patterns are similar and the flow becomes more disordered as a critical parameter is varied. However, we do find some significant differences. The flow regime in which the interfacial folds propagate self-similarly is not identified in their study. They observed that as the Stokes-Reynolds number, Re_S (which corresponds to *Gr* in our study) is increased Kelvin–Helmholtz instability is observed first and then and as Re_S is increased above a critical value ($Re_S \geqslant 5.25$) 'chaotic' instability, associated with interfacial breakup, is observed. They postulated that Rayleigh–Taylor instability leads to the breakup of the interface, while we observe that the interfacial breakup occurs because of Kelvin–Helmholtz instability.

This work was supported by the Microgravity Science Program of NASA.

REFERENCES

Bergholz, R. F. 1978 Instability of steady natural convection in a vertical fluid layer. *J. Fluid Mech.* **84**, 743–768.

Biringen, S. & Peltier, L. J. 1990 Numerical simulation of 3D Bénard convection with gravitational modulation. *Phys. Fluids* A **2**, 754–760.

Chen, C. F. & Chen, W. Y. 1999 Effect of gravity modulation on the stability of convection in a vertical slot. *J. Fluid Mech.* **395**, 327–344.

Christov, C. I. & Homsy, G. M. 2001 Nonlinear dynamics of two-dimensional convection in a vertically stratified slot with and without gravity modulation. *J. Fluid Mech.* **430**, 335–360.

Drolet, F. & Viñals, J. 1997 Onset of oscillatory instabilites under stochastic modulation. *Phys. Rev.* E **56**, 2649–2657.

Duval, W. M. B. 1992 The kinematics of buoyancy induced mixing. In *Proc. 8th European Symposium on Materials and Fluid Sciences in Microgravity*, pp. 855–861. ESA SP-333.

Duval, W. M. B. & Jacqmin, D. 1990 Interfacial dynamics of two fluids under an oscillating gravitational field. *AIAA J.* **28**, 1933–1941.

Farooq, A. & Homsy, G. M. 1996 Linear and non-linear dynamics of a differentially heated slot under gravity modulation. *J. Fluid Mech.* **313**, 1–38.

Gresho, P. M. & Sani, R. L. 1970 The effects of gravity modulation on the stability of a fluid layer. *J. Fluid Mech.* **40**, 783–806.

Jules, K., Hrovat, K., Kelly, E., McPherson, K. & Reckart, T. 2002 International space station increment-2 microgravity environment summary report. *Tech. Rep.* 211335. NASA.

Lele, S. K. 1992 Compact finfite difference schemes with spectral-like resolution. *J. Comput. Phys.* **103**, 16–42.

Lizée, A. & Alexander, J. 1997 Chaotic thermovibrational flow in a laterally heated cavity. *Phys. Rev.* E **56**, 4152–4156.

Ottino, J. M. 1982 Description of mixing with diffusion and reaction in terms of the concept of material surfaces. *J. Fluid Mech.* **114**, 83–103.

https://doi.org/10.1017/S0022112006001169 Published online by Cambridge University Press

Ottino, J. M. 1989 *The Kinematics of Mixing: Stretching, Chaos, and Transport*. Cambridge University Press.

Radcliffe, M., Steffen, J. E., Cook, E. L., Miller, J. F. C. L. R., Drake, M. C., Schroeder, F. S. & Stevens, J. R. 1988 Organic crystals in low earth orbit. *J. Cryst. Growth* **92**, 581–590.

Roache, P. J. 1982 *Computational Fluid Dynamics*. Hermosa.

Rogers, J. L., Schatz, M. F., Bougie, J. L. & Swift, J. B. 2000 Rayleigh-Bénard convection in avertically oscillated fluid layer. *Phys. Rev. Lett.* **84**, 87–90.

Sharp, D. H. 1984 An overview of Rayleigh-Taylor instability. *Physica* D **12**, 3–18.

Simpson, J. E. 1969 A comparison between laboratory and atmospheric density currents. *Q. J. R. Met. Soc.* **95**, 758–765.

Thomson, J., Casademunt, J., Drolet, F. & Viñals, J. 1997 Coarsening of solid-liquid mixtures in a random acceleration field. *Phys. Fluids* **9**, 1336–1343.

Tryggvason, G. 1988 Numerical simulations of the Rayleigh-Taylor instability. *J. Comput. Phys.* **75**, 253–282.

https://doi.org/10.1017/S0022112006001169 Published online by Cambridge University Press